A Rayleigh-Ritz solution for high order natural frequencies and eigenmodes of monopile supported offshore wind turbines considering tapered towers and soil pile interactions

Zhaolong Yu [a,b,*], Jørgen Amdahl [a,b]

[a] *Department of Marine Technology, Norwegian University of Science and Technology (NTNU), Norway*
[b] *Center for Autonomous Marine Operations and Systems (AMOS), Norwegian University of Science and Technology (NTNU), Norway*

A B S T R A C T

Offshore wind turbines may be exposed to extreme or accidental loads during the service life, such as extreme water slamming, ship collisions, earthquakes, extreme winds, ice loads, etc. Under the action of such loads, they will respond not only in the primary eigenmode, but also high order modes. This paper presents a Rayleigh-Ritz solution for high order natural frequencies and eigenmodes of monopile supported offshore turbines. The model considers explicitly tapered wind turbine towers and soil-pile interactions. Different soil conditions are considered using equivalent cross coupled springs at the mudline. The proposed Rayleigh-Ritz solution is applied to the DTU 10 MW wind turbine mounted on a monopile foundation. The predicted natural frequencies and eigenmodes are compared with nonlinear finite element simulations using USFOS. The results show excellent agreement for the first 3 eigenmodes. Even higher eigenmodes than the 3rd order are also calculated but are not presented. They can be readily obtained if needed.

High order natural frequencies and eigenmodes using the proposed Rayleigh-Ritz solution can, together with the Duhamel's integral, be well utilized in the buckling and collapse analysis and design of monopile supported offshore wind turbines in Ultimate Limit States (ULS) and Accidental Limit States (ALS). In addition, the high accuracy of the predicted primary natural frequency makes it a useful design tool to help avoid undesired resonance from external excitation loads and to reduce resonance related fatigue effects in Fatigue Limit States (FLS).

1. Introduction

Wind power is at the forefront of the energy evolution transitioning from classical fossil fuel to clean and decarbonizing energy. According to DNV report [1], electricity will increase from less than 20% of the energy mix today to around 40% by 2050, where wind power will account for a substantial share of about 30% of total electricity. Wind power is generally harvested by onshore and offshore wind turbines. Compared to onshore turbines, offshore wind turbines (OWTs) can utilize the vast free space in the open sea with higher wind speeds for electricity generation and fewer problems related to noises. Offshore wind turbines need to be supported by either fixed foundations (monopile, jacket, etc) or floating floaters (semi-submersible, Spar, barge, tension leg, etc), among which the monopile foundation design has proven itself to be the most cost-effective support structure in shallow water ($<40~m$) and even for

---

deeper waters or larger turbines to come. In addition, monopile foundations are relatively easy to fabricate and to install. According to Ramirez et al. [2], large diameter monopiles account for more than 80% of newly installed offshore turbine foundations in Europe.

Offshore wind turbines are dynamically sensitive structures, and the dynamics of OWTs must be studied in order to avoid resonance arising from external excitations and the resonance related fatigue damage through dynamic amplification of turbine responses. Evaluation of the primary natural frequency of OWTs is therefore an important design parameter in rules and standards (DNV–OS–J101 [3], IEC-61400-1 [4], etc). Typical natural frequency range of OWTs shall be designed away from the rotor rotational frequency (1 P) and the blade passing frequency (2 P/3 P) as well as the predominant excitation frequency from waves and winds. Arany et al. [5] showed typical loading spectra from waves and winds at offshore sites and the range of 1 P and 3 P frequencies for a number of commercial wind turbines of different capacities (2–8 MW) in Fig. 1. The so-called soft-stiff design is most widely adopted, where the primary frequency of OWTs fall in the frequency gap between 1 P and 3 P.

In addition to the primary natural frequency, high order natural frequencies and eigenmodes become important when OWTs are subjected to extreme or accidental loads in ULS and ALS conditions, such as extreme water slamming, ship collisions, earthquakes, extreme winds, ice loads, etc. In 2013, Super typhoon Usagi on category 4 impacted a wind farm on the southeast coast of China with a dramatic change of wind direction and a maximum wind speed of 57 m/s at a 10-m elevation. As a result, eight turbine towers collapsed, eleven rotor blades broke off and three turbines were burned, leading to an approximate $16 million loss to the wind farm [6]. Fig. 2(a) shows typical buckling and collapsing patterns of wind turbines after extreme storms. Just recently in 2022, a cargo ship of 37,200 tons was cast adrift by a heavy storm into the Hollandse Kust Zuid offshore wind farm area in the Dutch North Sea [7]. The ship collided with a monopile foundation of an offshore turbine causing significant dents (refer Fig. 2(b)) on the monopile, which needs to be removed afterwards. Such extreme and accidental actions are often characterized by loads with short durations and large amplitudes, and the responses of OWTs are highly transient involving several high order eigenmodes [8,9]. It is therefore crucial to accurately assess high order natural frequencies and eigenmodes of OWTs in addition to the first one for reliable analysis and design of OWTs in ULS and ALS conditions.

This paper presents a high-fidelity Rayleigh-Ritz solution for high order natural frequencies and eigenmodes of monopile supported offshore turbines considering explicitly tapered turbine towers and soil-pile interactions. The DTU 10 MW turbine mounted on a monopile foundation is used as an example. Different soil conditions are considered using equivalent cross coupled springs at the mudline. Natural frequencies and eigenmodes obtained by the derived Rayleigh-Ritz solution are verified using nonlinear finite element analysis in USFOS. The proposed Rayleigh-Ritz solutions are formulated in matrix form, and can be conveniently implemented in the FLS, ULS and ALS analysis and design of offshore wind turbines.

2. Existing simplified models for monopile supported offshore wind turbines

2.1. Rigid base model

The primary natural frequency of offshore wind turbines is of interest to avoid resonance from external excitation loads. As a first estimation of the first natural frequency, offshore wind turbines are often simplified as a uniform cantilever beam rigidly supported at the base with a concentrated mass at the beam head representing mass of the rotor, nacelle, and an equivalent mass of the turbine tower as shown in Fig. 3(a) and (b). The rigid base tower natural frequency $f_{RB,T}$ can be expressed as:
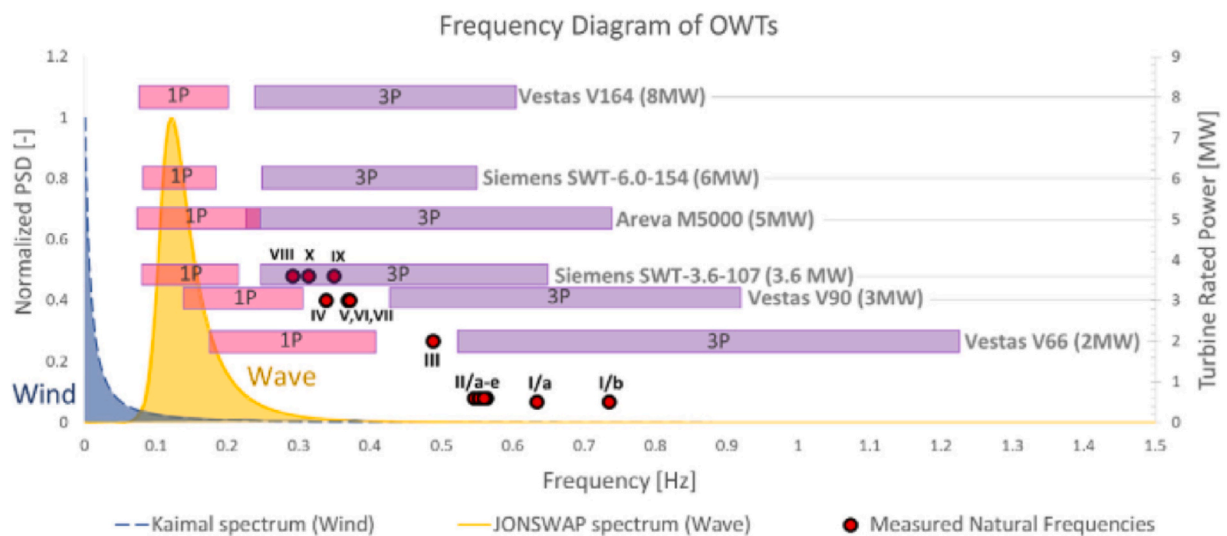

Fig. 1. Typical wind and wave spectra, rotor rotational frequency (1 P) and blade passing frequency (3 P) bands for six commercial turbines, from Arany et al. [5].
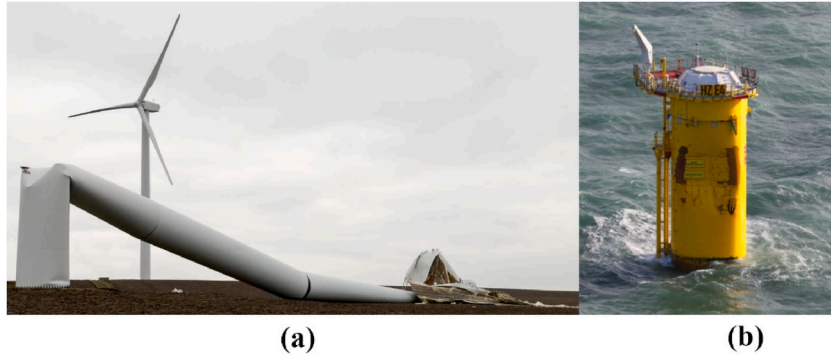
Fig. 2. (A) Buckling and collapse of a wind turbine after extreme winds [10]; (b) damaged monopile foundation of an offshore turbine foundation after being collided by a drifting cargo ship of 37,200 tons in heavy storms [7].

$$f_{RB,T} = \sqrt{\frac{k_T}{m_{RNA} + \mu m_T}} \tag{1}$$

Where $k_T = 3E_T I_T/L_T^3$ is the lateral stiffness of the tower, E_T, I_T and L_T are Young's modulus of the tower material, cross sectional moment of inertia and length of the tower, respectively. m_{RNA} is the mass of the rotor-nacelle assembly (RNA), and m_T is the mass of the tower. μ is the equivalent mass ratio of the tower concentrated at the tower top. Arany et al. [5] suggested that the uniform tower diameter D_T should be taken as an average of the top and the bottom diameter of the tower $D_T = (D_{Tt} + D_{Tb})/2$. The average tower thickness was therefore determined by $t_T = m_T/(\pi \rho_T D_T L_T)$, where ρ_T is the density the turbine tower material.

The selected equivalent mass ratio μ varies in the literature. DNV–OS–J101 [3] suggests $\mu = 0.25$ for earthquake analysis of offshore wind turbines using response spectrum methods. IEC-61400-1 (2005) [11] recommends $\mu = 0.50$ to establish accelerations at the first tower bending eigen-frequency for the design response spectrum in earthquake analysis. The latest version of IEC-61400-1 (2019) [4] however suggests using a simplified multi-degree of freedom system for the calculation of wind turbine structural responses. When the static deflection shape of a beam subjected to a concentrated load at the beam tip is used as shape functions, $\mu = \frac{33}{140} = 0.236$ is obtained. The recommended mass ratio by DNV–OS–J101 [3] is close to this analytical value. Van der Tempel and Molenaar [12] presented a similar expression of $f_{RB,T} = \sqrt{\frac{3.04E_T I_T}{(m_{RNA} + 0.227 m_T)L_T^3}}$ for the first natural frequency of wind turbine towers.

When monopile foundations are considered, Arany et al. [5] calculated the lateral stiffness of the monopile-tower system shown in Fig. 3(d), and the fixed-base natural frequency of the tower-monopile system (excluding foundation stiffness) is given by:

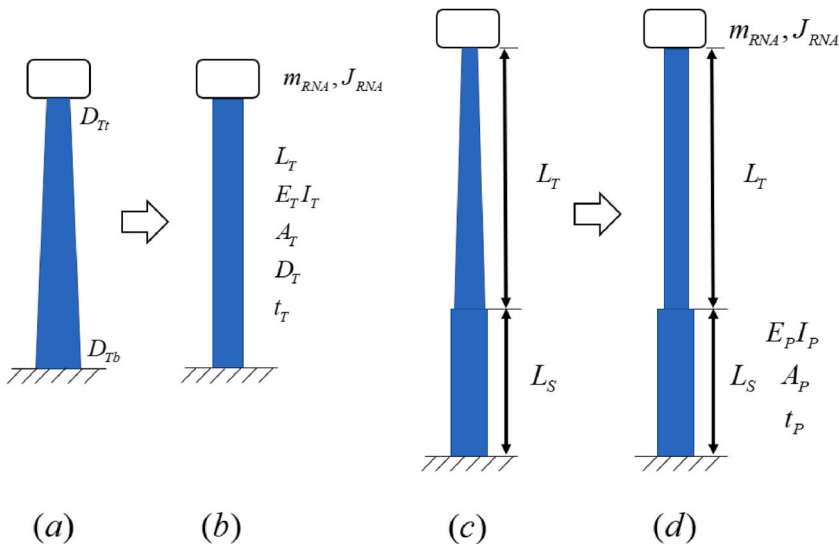$$f_{RB} = \sqrt{\frac{1}{1 + (1+\lambda)^3 \chi - \chi}} f_{RB,T} \tag{2}$$

Fig. 3. Simplified models for offshore wind turbines with rigid bases.

where $\chi = \frac{E_T I_T}{E_P I_P}$ is the bending stiffness ratio of the tower and the pile, $\lambda = L_S/L_T$ is the ratio of the pile length above the mudline and the tower length as shown in Fig. 3(d). E_P, I_P and L_S are Young's modulus of the pile material, cross sectional moment of inertia and the length of the monopile above the mudline, respectively. Ko [13] considered further the influence of tapered towers with varying cross sections in the evaluation of the primary eigenfrequency of monopile wind turbines.

Ladeira et al. [9] used the Idealized Structural Unit Method (ISUM) to model the tower-monopile system, where a monopile supported wind turbine was divided into a few elements with uniform cross sections, and the terms from exact beam solutions were used as interpolation functions. Continuity and compatibility conditions were satisfied at the element interfaces. In this way, high order natural frequencies and eigenmodes could be established.

2.2. Modelling soil-pile interactions

For dynamic analysis of monopile supported offshore wind turbines, appropriate stiffnesses for the foundation structure shall be applied. The soil stiffness is often represented by nonlinear P-y curves along the embedded depth for the lateral stiffness and nonlinear T-z and Q-z curves for the axial stiffness. The approach can be found in API-RPGEO [14] and is recommended in DNV-ST-0126 [15]. Due to the stochastic nature of measured soil properties, high or low estimates of the involved soil parameters shall be applied for different design process targets to account for their uncertainties [3]. The nonlinear P-y curve method was initially designed for long flexible piles and had worked well for such conditions. However, its direct application to low length-to-diameter ratio monopiles (often less than 10 to 15) may give unsatisfactory results [16]. Another approach is to model soil-pile interactions by finite element methods [17], where the soil part is modelled as constitutive material models (e.g. Mohr-Coulomb material) with detailed soil properties and distributions.

In the initial design stage, detailed information of nonlinear soil stiffness is often not available and such analysis is often very time consuming. In the absence of sophisticated modelling tools, simplified representation of the foundation stiffness becomes relevant. Three approaches [18] are often used to represent monopile foundation stiffnesses: the distributed springs (DS) model, the apparent fixity (AF) model and the coupled spring (CS) model as shown in Fig. 4. The DS model (Fig. 4(a)) idealizes the monopile with flexible foundation as a free-free beam with a set of elastic springs distributed along the embedded length of the monopile. The soil stiffnesses are linearized from the original nonlinear P-y curves. The AF model (Fig. 4(b)) idealizes the monopile with flexible foundation as a cantilever beam whose properties are different above and below the mudline. The beam below the mudline has effective properties and a fictitious length that is tuned to obtain the same mudline displacement and rotation as those obtained using the high-fidelity P-y curves. The CS model (Fig. 4(c)) idealizes the monopile foundation stiffness as a set of cross-coupled translational and rotational springs positioned at the mudline (see Eq. (3)). The mudline stiffnesses are determined such that the same mudline displacement ρ and rotation θ are obtained as with the P-y model.

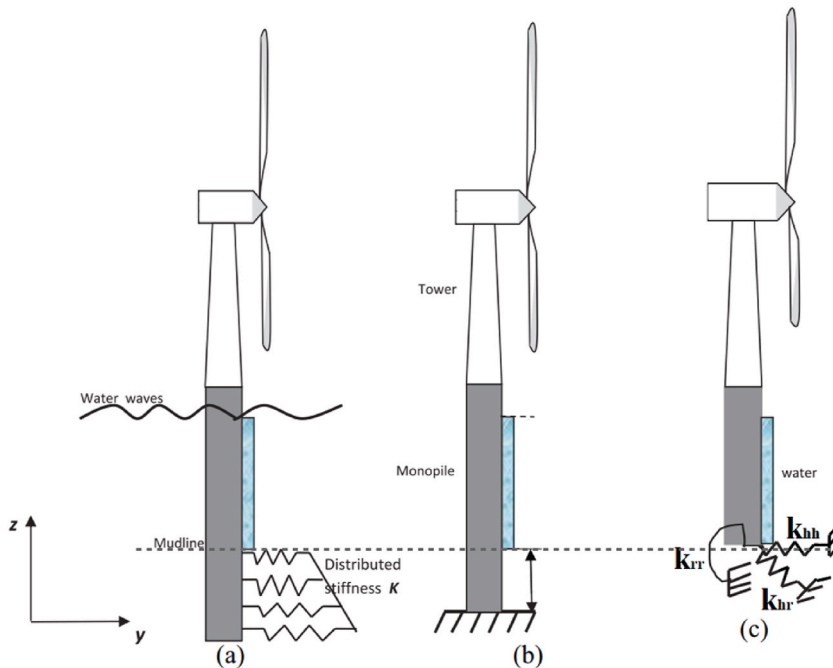
Fig. 4. Three simplified approaches to model the monopile foundations: (a) the distributed springs (DS) model; (b) the apparent fixity (AF) model; and (c) the coupled spring (CS) model. The figure is reproduced from Robinson and Wang [21].

$$\begin{bmatrix} F \\ M \end{bmatrix} = \begin{bmatrix} k_{hh} & k_{hr} \\ k_{rh} & k_{rr} \end{bmatrix} \begin{bmatrix} \rho \\ \theta \end{bmatrix} \tag{3}$$

The three simplified models have been used and discussed extensively in the literature. Zaaijer [19] discussed the accuracy of different simplified foundation modelling techniques in the assessment of dynamic behavior of monopile offshore wind turbines and showed that the coupled spring model gave the best solution for monopiles while the AF model yielded large sensitivity of the predicted natural frequencies to the effective fixity length and was therefore strongly discouraged. The prediction with uncoupled spring models gave large deviations from the reference model and was not recommended. Arany et al. [20] reached similar conclusions. They presented an analytical model for the first natural frequency of monopile offshore wind turbines assuming uniform cross sections and coupled springs as the foundation stiffness. The cross-coupling term was shown to have significant effects on the predicted natural frequencies.

The literature review showed that the coupled spring model is a very promising approach to model the foundation. Arany et al. [5] considered a three-term coupled spring model in the evaluation of the first natural frequency. Two empirical flexibility factors were introduced, and they shall be multiplied by the first natural frequency f_{RB} in Eq. (2) to account for the effects of foundation stiffnesses. Determination of the foundation stiffnesses is however challenging in view of the complicated soil composition and distributions along the depth. Two main parameters are found to govern the calculation methodology of foundation stiffnesses [5], (1) site condition and ground profile at site; (2) pile slenderness and rigidity. Given the information of ground/soil profiles and pile properties, it is possible to classify the pile behavior, i.e., whether the monopile will behave as a long flexible pile or a short rigid pile, and then to use appropriate relations to obtain the stiffness terms K_{hh}, K_{rr} and K_{hr}.

According to Randolph [22], the pile is considered as a long flexible pile if $\frac{L_P}{D_P} \geq \left(\frac{E_{Pe}}{G^*}\right)^{\frac{2}{7}}$ and as rigid if $\frac{L_P}{D_P} \leq 0.05\left(\frac{E_{Pe}}{G^*}\right)^{\frac{1}{2}}$ [23], where L_P and D_P are the length and diameter of the embedded pile, $E_{Pe} = E_P I_P/(\pi D_P^4/64)$ is the equivalent Young's modulus, $G^* = G_s(1+3/4\nu_s)$ is the effective shear stress of the soil, G_s is the soil shear modulus and ν_s is the soil's Poisson ratio. Poulos and Davis [24] introduced a characteristic pile slenderness parameter $\beta_{\text{pile}} = \sqrt[4]{\frac{k_{sub}D_P}{4E_P L_P}}$ and suggested that the pile can be considered as slender when $\beta_{\text{pile}}L_P > 2.5$ and rigid when $\beta_{\text{pile}}L_P < 1.5$, where k_{sub} is the subgrade reaction modulus of the soil.

In the absence of detailed and careful site measured soil data, a number of analytical and empirical formulations are available in the literature by assuming certain soil stiffness profiles, e.g. Randolph [22], Shadlou and Bhattacharya [16], Carter and Kulhawy [23], etc. An overview of formulations for the pile foundation stiffness is found in Arany et al. [25]. Arany et al. [25] stated that slender pile formulae often produce better approximation of the eigen frequencies of structures than formulae for rigid piles. The foundation stiffness formulations suggested by Shadlou and Bhattacharya [16] considering low length-to-diameter ratios of monopiles exhibiting flexible and rigid behavior are given in Table 1 and are used in **Section 3.4**.

$f(\nu_s) = 1 + 0.6|\nu_s - 0.25|$ is recommended by Shadlou and Bhattacharya [16]. E_{SO} is the soil Young's modulus.

3. A Rayleigh-Ritz solution for monopile supported offshore turbines

3.1. The Rayleigh-Ritz formulation

The structural deflection shape can generally be considered as a superposition of a number of linearly independent modes:

$$\frac{w(z)}{L} = \sum_{i=1}^{n} a_i \varphi_i(z) \tag{4}$$

where φ_i is the i_{th} trial function and a_i is the corresponding weight. L is the characteristic length of the structure.

The Rayleigh principle states that the frequencies for a conservative system that oscillates about an equilibrium state have sta-

Table 1
Foundation stiffness of piles exhibiting flexible and rigid behaviors from Shadlou and Bhattacharya [16].

Pile behavior	Soil model	$\dfrac{k_{hh}}{f(\nu_s)E_{SO}(D_P/2)}$	$-\dfrac{k_{hr}}{f(\nu_s)E_{SO}(D_P/2)^2}$	$\dfrac{k_{rr}}{f(\nu_s)E_{SO}(D_P/2)^3}$
Flexible	Homogeneous	$2.9\left(\frac{E_P}{E_{SO}}\right)^{0.186}$	$1.2\left(\frac{E_P}{E_{SO}}\right)^{0.5}$	$1.5\left(\frac{E_P}{E_{SO}}\right)^{0.73}$
	Parabolic Inhomogeneous	$2.03\left(\frac{E_P}{E_{SO}}\right)^{0.27}$	$1.17\left(\frac{E_P}{E_{SO}}\right)^{0.52}$	$1.42\left(\frac{E_P}{E_{SO}}\right)^{0.76}$
	Linear inhomogeneous	$1.58\left(\frac{E_P}{E_{SO}}\right)^{0.34}$	$1.07\left(\frac{E_P}{E_{SO}}\right)^{0.567}$	$1.38\left(\frac{E_P}{E_{SO}}\right)^{0.78}$
Rigid	Homogeneous	$6.4\left(\frac{L_P}{D_P}\right)^{0.62}$	$7.1\left(\frac{L_P}{D_P}\right)^{1.56}$	$13.2\left(\frac{L_P}{D_P}\right)^{2.5}$
	Parabolic Inhomogeneous	$5.33\left(\frac{L_P}{D_P}\right)^{1.07}$	$7.2\left(\frac{L_P}{D_P}\right)^{2}$	$13\left(\frac{L_P}{D_P}\right)^{3}$
	Linear inhomogeneous	$4.7\left(\frac{L_P}{D_P}\right)^{1.53}$	$7.1\left(\frac{L_P}{D_P}\right)^{2.5}$	$12.7\left(\frac{L_P}{D_P}\right)^{3.45}$

tionary values when the system vibrates in its eigenmodes [26]. The Rayleigh-Ritz quotient $R(a_1, a_2, \cdots a_n)$ is expressed as:

$$R(a_1, a_2, \cdots a_n) = \omega^2 = \frac{U_{\max}(a_1, a_2, \cdots a_n)}{T_0(a_1, a_2, \cdots a_n)} \tag{5}$$

where ω is the vibration frequency, $U_{\max}$ is the maximum strain energy and $T_{\max} = \omega^2 T_0$ is the maximum kinetic energy. The Rayleigh-Ritz quotient shall be minimized with respect to the coefficients, resulting in the following expression:

$$\frac{\partial R(a_1, a_2, \cdots a_n)}{\partial a_i} = 0, i = 1, 2, \cdots n \Rightarrow \left(\frac{\partial U_{\max}}{\partial a_i} - \omega^2 \frac{\partial T_0}{\partial a_i} \right) = 0 \quad i = 1, 2, \cdots n \tag{6}$$

Eq. (6) leads to the final expression with respect to the generalized stiffness matrix $\mathbf{K}$ and the generalized mass matrix $\mathbf{M}$:

$$(\mathbf{K} - \omega^2 \mathbf{M})\mathbf{a} = \mathbf{0} \tag{7}$$

Nontrivial solutions exist when the matrix determinant vanishes. This determines the weight coefficients $a_1, a_2, \cdots a_n$, and thereby the natural frequencies and eigenmodes. In this paper, we adopt a power series of trial functions of n_{th} order for turbine structures as follows:

$$\varphi_0 = 1, \varphi_1 = \frac{z}{L}, \varphi_2 = \left(\frac{z}{L}\right)^2, \varphi_3 = \left(\frac{z}{L}\right)^3 \cdots, \varphi_n = \left(\frac{z}{L}\right)^n \tag{8}$$

3.2. High order natural frequencies and eigenmodes for a uniform cantilever beam with a tip mass

Land based wind turbines may be simplified as a uniform beam with a concentrated mass at the top and a rigid base at the bottom (see Fig. 3(a) and (b)) as a first rough approximation [5,13]. This may also be applied for offshore wind turbine towers or monopile supported offshore turbines. Following Arany et al. [5], the uniform tower diameter D_T is taken as an average of the top and the bottom diameters of the tower $D_T = (D_{Tt} + D_{Tb})/2$. The average tower thickness is determined by $t_T = m_T/(\pi \rho_T D_T L_T)$, where m_T is the tower total weight, ρ_T, D_T and L_T are the density, diameter and length of the turbine tower, respectively.

Analytical solutions of the natural frequencies and eigenmodes exist for a uniform beam with a tip mass rigidly fixed at the base, (see Erturk and Inman [27]), where the natural frequencies are determined by solving Eq. (9) with respect to λ_ω:

$$1 + \cos \lambda_\omega \cosh \lambda_\omega + \lambda_\omega \frac{m_{RNA}}{mL} \left(\cos \lambda_\omega \sinh \lambda_\omega - \sin \lambda_\omega \cosh \lambda_\omega \right) - \frac{\lambda_\omega^3 J_{RNA}}{mL^3} \left(\cosh \lambda_\omega \sin \lambda_\omega + \sinh \lambda_\omega \cos \lambda_\omega \right)$$
$$+ \frac{\lambda_\omega^4 m_{RNA} J_{RNA}}{m^2 L^4} \left(1 - \cos \lambda_\omega \cosh \lambda_\omega \right) = 0 \tag{9}$$

$m = \rho A$ is the beam mass per unit length. m_{RNA} and J_{RNA} are the mass and the rotational inertia of the top mass. The natural frequencies can be found by $\omega = \sqrt{\frac{\lambda_\omega^4 EI}{mL^4}}$.

The corresponding r_{th} eigenmode is:

$$\varphi_r(x) = A_r \left[\cos \frac{\lambda_{\omega,r} x}{L} - \cosh \frac{\lambda_{\omega,r} x}{L} + \frac{\sin \lambda_{\omega,r} - \sinh \lambda_{\omega,r} + \lambda_{\omega,r} \frac{m_{RNA}}{mL} \left(\cos \lambda_{\omega,r} - \cosh \lambda_{\omega,r} \right)}{\cos \lambda_{\omega,r} + \cosh \lambda_{\omega,r} - \lambda_{\omega,r} \frac{m_{RNA}}{mL} \left(\sin \lambda_{\omega,r} - \sinh \lambda_{\omega,r} \right)} \left(\sin \frac{\lambda_{\omega,r} x}{L} - \sinh \frac{\lambda_{\omega,r} x}{L} \right) \right] \tag{10}$$

A_r is a single modal constant.

The analytical solutions can be used to check the accuracy of the Rayleigh-Ritz approach with different polynomial orders. Using the Rayleigh-Ritz approach, the maximum strain energy $U_{\max}$ is expressed as:

$$U_{\max} = \frac{1}{2} \int_0^{L_T} E_T I_T \left[\frac{d^2 w(z)}{dz^2} \right]^2 dz$$
$$= \frac{1}{2} \sum_{i=1}^{n} \sum_{j=1}^{n} K_{ij} L_T^2 a_i a_j, \text{ where } K_{ij} = \int_0^{L_T} E_T I_T \frac{d^2 \varphi_i(z)}{dz^2} \frac{d^2 \varphi_j(z)}{dz^2} dz \tag{11}$$

The kinetic energy (KE) T_0 includes three terms and reads:

$$T_0 = \underbrace{\frac{1}{2} \int_0^{L_T} m[w(z)]^2 dx}_{\text{tower KE}} + \underbrace{\left[\frac{1}{2} m_{rna} [w(z)]^2 \right]_{z=L_T}}_{\text{RNA mass KE}} + \underbrace{\left[\frac{1}{2} J_{rna} \left[\frac{dw(z)}{dz} \right]^2 \right]_{z=L_T}}_{\text{RNA rotational inertia KE}}$$
$$= \frac{1}{2} \sum_{i=1}^{n} \sum_{j=1}^{n} M_{ij} L_T^2 a_i a_j, \text{ where } M_{ij} = \int_0^{L_T} m \varphi_i(z) \varphi_j(z) dz + m_{rna} \varphi_i(L_T) \varphi_j(L_T) + \left[J_{RNA} \frac{d\varphi_i(z)}{dz} \frac{d\varphi_j(z)}{dz} \right]_{z=L_T} \tag{12}$$

The first term in Eq. (12) is the kinetic energy carried by the distributed tower mass, and the latter two terms are kinetic energy

contributions from the translational mass and the rotational inertia of the top RNA, respectively. $\mathbf{K_{ij}}$ and $\mathbf{M_{ij}}$ are the generalized stiffness matrix and the generalized mass matrix, respectively. With Eq. (7), the natural frequencies and eigenmodes are readily obtained.

The well-established turbine tower of a 5 MW reference wind turbine defined by National Renewable Energy Laboratory (NREL) is selected as an example [28]. The main structural parameters of the turbine tower are given in Table 2. Natural frequencies and eigenmodes of the wind turbine with different support structures are well documented by Bir and Jonkman [18]. The Rayleigh-Ritz approach with polynomials of 3rd and 4th order are selected. The obtained natural frequencies are compared in Table 3 and the eigenmodes are compared in Fig. 5.

For wind turbines subjected to extreme loads, the first three eigenmodes are generally of interest. From Table 3 and Fig. 5, the Rayleigh-Ritz method with a complete 4th order polynomial can provide excellent prediction of tower eigenfrequencies and eigenmodes. The differences with analytical solutions are within 2%. The Rayleigh-Ritz method with a complete 3rd order polynomial can only provide the first two eigenmodes. The first eigenfrequency is well predicted while there is a 5.4% difference for the 2nd eigenfrequency. It is therefore recommended to use the 4th order polynomial terms for the first 3 modes and the corresponding stiffness and mass matrices are given in Appendix A.

Simplification of the tapered turbine tower into an equivalent uniform beam with a tip mass introduces errors. Table 3 shows that absolute differences of the natural frequencies are in the range of 10%–15% for all the first 3 modes, which is only acceptable as a first crude estimation.

3.3. High order natural frequencies and eigenmodes for a tapered turbine tower

Tapered towers with varying cross section diameters and thicknesses along the height shall be included for a more accurate representation of high order natural frequencies and eigenmodes. This will be useful for both land-based turbines (Fig. 6(a)) and floating offshore wind turbines (Fig. 6(b)). A rotational spring is introduced at the bottom to represent finite rotational stiffness. The spring represents the foundation stiffness for land-based turbines and the rotational flexibilities of the floater structure at the tower connection for floating wind turbines.

Variations of the cross-section moment of inertia and cross section area of turbine towers are studied using two representative turbine designs: the NREL 5 MW turbine tower and the DTU 10 MW turbine tower. The main structural parameters of the NREL 5 MW turbine tower are given in Table 2. The DTU 10 MW reference wind turbine tower is developed by Bak et al. [29] for a land based turbine. The tower thickness is increased by 20% in Bachynski and Ormberg [30] in order to be mounted on a monopile foundation without undesired resonance. The latter is adopted in this study and the main structural parameters for the modified DTU 10 MW turbine tower is given in Table 4.

The cross-sectional moment of inertia and area for the two reference turbine towers are plotted in Fig. 7. In the calculation of equivalent bending stiffness, Arany et al. [5] assumed a linear variation of tower diameters and thereby a distribution of cross section moments of inertia as $I_T = I_{Tt}(1 + az)^3$, where I_{Tt} is the cross section moment of inertia at the tower top, z is the tower coordinate along its height and a is a constant. Ko [13] compared different formulations of representing variations of the tower moment of inertia and proposed to approximate the cross-section moment of inertia as $\frac{I_{T(z)}}{I_{Tb}} = \left(\frac{I_{Tt}}{I_{Tb}}\right)^{\frac{z}{L_T}}$, where I_{Tb} is the cross-section moment of inertia at the tower bottom. Both models were however, not able to capture well the variations for the NREL 5 MW tower according to results in Ko [13]. In addition, the expressions are not very convenient to integrate mathematically. To improve the estimation accuracy, a 2nd order polynomial is adopted to approximate the variations of moment of inertia while a 1st order polynomial is used for cross section area approximation as follows.

$$\frac{I_T}{I_{Tb}} = b_0 + b_1 \frac{z}{L} + b_2 \left(\frac{z}{L}\right)^2 \tag{13}$$

$$\frac{A_T}{A_{Tb}} = c_0 + c_1 \frac{z}{L} \tag{14}$$

where b_0, b_1, b_2 and c_0, c_1 are approximation constants for the cross-sectional moment of inertia and area, respectively, and they should be determined by minimizing the deviations from the raw data points. For the DTU 10 MW tower, the following coefficients are obtained: $b_0 = 0.9955$,

Table 2
Structural parameters of the NREL 5 MW reference wind turbine [28].

Tower length L_T	87.6 m	Average tower diameter D_T	4.935 m
Tower total mass $\mathbf{m_T}$	347,460 kg	Average tower thickness t_T	0.0301 m
Tower top diamter $\mathbf{D_{Tt}}$	3.87 m	Young's modulus $\mathbf{E_T}$	210 Gpa
Tower top thickness	0.0247 m	Tower material density $\mathbf{\rho_T}$	8500 kg/m^3
Tower bottom diameter $\mathbf{D_{Tb}}$	6.0 m	RNA total mass $\mathbf{m_{RNA}}$	350,000 kg
Tower bottom thickness	0.0351 m	RNA rotational inertia $\mathbf{J_{RNA}}$	4.37×10^7 kgm^2

Table 3
Natural frequencies [HZ]of the NREL 5 MW reference wind turbine with fixed base.

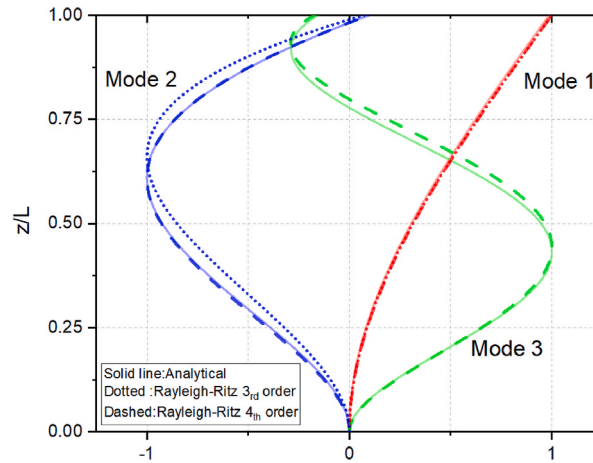| Mode (Hz)	analytical	R–R 3rd order	Error	R–R 4th order	Error	Bir and Jonkman [18] with tapered tower	Error
1st mode	0.2754	0.2754	0.00%	0.2753	0.04%	0.3188	−13.61%
2nd mode	2.1264	2.2410	5.39%	2.1278	0.07%	1.8820	12.99%
3rd mode	5.2312	x	x	5.2931	1.18%	4.7244	10.73%

Fig. 5. First three eigenmodes of the simplified NREL 5 MW turbine tower with a rigid base.
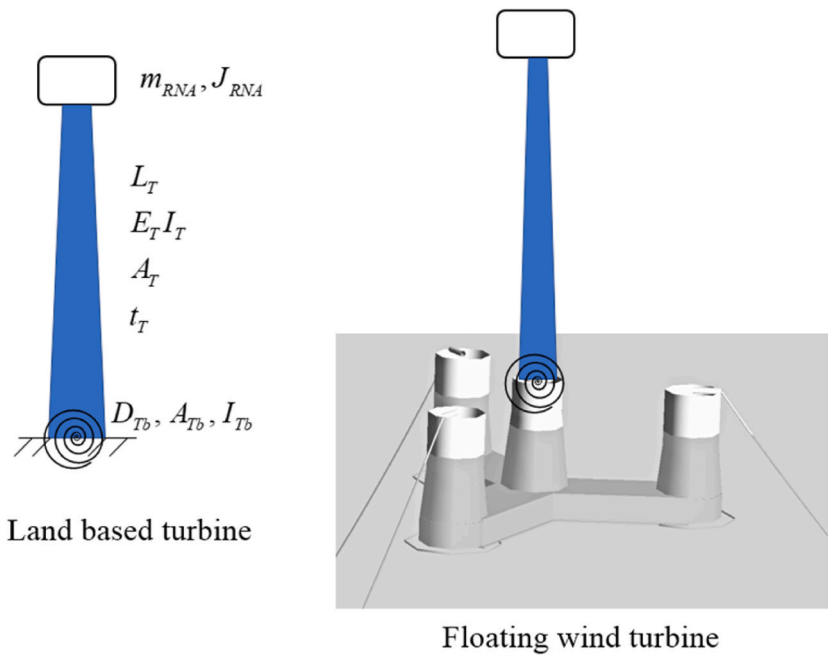

Fig. 6. Simplified turbine tower model with varying cross sections and finite end rotation stiffness.

$B_1 = -1.4522$, $b_2 = 0.6101$, $c_0 = 0.9684$ and $c_1 = -0.6710$. The resulting fitted curves are shown in Fig. 7. It is found that the 2nd order polynomials yield excellent fit of the tower moment of inertia while the tower area is represented reasonably well by the 1st order polynomial.

Using the Rayleigh-Ritz approach, the maximum strain energy U_{max} and the kinetic energy T_0 are expressed as:

Table 4
Structural parameters of the DTU 10 MW reference wind turbine tower [29].

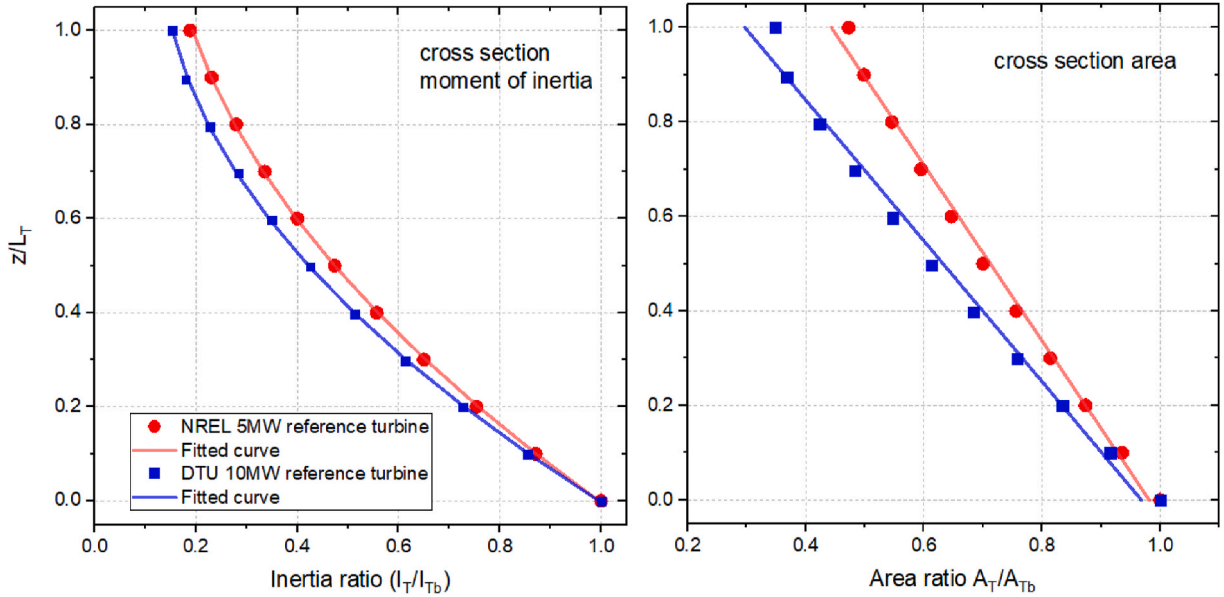| Tower length L_T	115.63 m	Young's modulus E_T	210 Gpa
Tower total mass $\mathbf{m_T}$	628 tons × 1.2	Tower material density ρ_T	8500 kg/m³
Tower top diamter $\mathbf{D_{Tt}}$	5.5 m	RNA total mass $\mathbf{m_{RNA}}$	674 tons
Tower top thickness	0.020 m × 1.2	RNA rotational inertia J_{RNA}	1.659×10^8 kgm²
Tower bottom diameter $\mathbf{D_{Tb}}$	8.3 m	Moment of inertia at tower bottom cross section $\mathbf{I_{Tb}}$	10.07 m⁴
Tower bottom thickness	0.038 m × 1.2		

Fig. 7. Fitting of tower cross section moment of inertia and area according to Eqs. (13) and (14).

$$U_{\max} = \frac{1}{2}\int_0^{L_T} E_T I_T \left[\frac{d^2w(z)}{dz^2}\right]^2 dz + \frac{1}{2}k_{rot}\left[\frac{dw(z)}{dz}\right]^2_{z=0}$$
$$= \frac{1}{2}\sum_{i=1}^n \sum_{j=1}^n K_{ij}L_T^2 a_i a_j, \text{ where } K_{ij} = \int_0^{L_T} E_T I_T(z)\frac{d^2\varphi_i(z)}{dz^2}\frac{d^2\varphi_j(z)}{dz^2}dz + k_{rot}\left[\frac{d\varphi_i(z)}{dz}\frac{d\varphi_j(z)}{dz}\right]_{z=0} \tag{15}$$

$$T_0 = \frac{1}{2}\int_0^{L_T} \rho A_T(z)[w(z)]^2 dz + \left[\frac{1}{2}m_{RNA}[w(z)]^2\right]_{z=L_T} + \left[\frac{1}{2}J_{RNA}\left[\frac{dw(z)}{dz}\right]^2\right]_{z=L_T}$$
$$= \frac{1}{2}\sum_{i=1}^n \sum_{j=1}^n M_{ij}L_T^2 a_i a_j, \text{ where } M_{ij} = \int_0^{L_T} \rho A_T \varphi_i(z)\varphi_j(z)dz + m_{RNA}\varphi_i(L_T)\varphi_j(L_T) + \left[J_{RNA}\frac{d\varphi_i(z)}{dz}\frac{d\varphi_j(z)}{dz}\right]_{z=L_T} \tag{16}$$

Where $I_T(z)$ and $A_T(z)$ are the moment of inertia and area of the tower cross sections that vary along the height according to Eqs. (13) and (14), and k_{rot} is the rotational stiffness at the tower base or the connection.

Considering a 2nd order polynomial approximation for the cross-section moment of inertia in addition to the uniform beam formulation, we select a complete 6th order polynomials as trial functions for the tapered tower, and the resulting stiffness matrix and mass matrix are given in **Appendix B**. Rayleigh Ritz solutions with complete 4th and 5th order polynomials are also presented to enable a comparison. The corresponding mass and stiffness matrices can be readily obtained by removing the corresponding rows and columns from the matrices for the 6th order.

To validate the Rayleigh-Ritz prediction, nonlinear finite element software USFOS is adopted to model the modified DTU 10 MW turbine tower and to evaluate its natural frequencies and eigenmodes. USFOS [31] is a program aimed at ultimate strength and progressive collapse analysis of framed offshore structures. The basic idea of the program is to use terms from analytical beam solutions in the shape functions so that one physical element in the structure can be represented by one finite element, which is efficient but still

Table 5
Natural frequencies [HZ] of the modified DTU 10 MW reference turbine tower with rigid base.

Mode (Hz)	USFOS with J_{RNA}	R–R method of 6th order with J_{RNA}	Error	R–R method of 5th order with J_{RNA}	R–R method of 4th order with J_{RNA}
1st mode	0.282	0.281	−0.4%	0.281	0.281
2nd mode	1.444	1.441	−0.2%	1.441	1.441
3rd mode	3.490	3.639	4.3%	3.639	3.911
Mode (Hz)	USFOS without J_{RNA}	R–R method of 6th order without J_{RNA}	Error	R–R method of 5th order without J_{RNA}	
1st mode	0.289	0.288	−0.3%	0.288	0.288
2nd mode	2.420	2.474	2.2%	2.476	2.566
3rd mode	6.817	7.383	8.3%	7.978	8.898

preserves high accuracy. Nonlinear material properties are accounted for by means of yield hinge theory and interaction formulas for stress resultants. USFOS has been extensively used in the analysis of framed structures under environmental and accidental loads, such as offshore wind turbines [32], jackets and jack-ups [33], floating bridges [34] and offshore fish farms [35]. The DTU 10 MW reference turbine tower is modelled using 20 beam elements. Within each element, cross sections with linearly varying diameters can be modelled. The rotor-nacelle-assembly is modelled as a nodal mass including rotational inertia J_{RNA} at the top.

The tower bottom is considered fixed in the first place. The calculated natural frequencies from USFOS simulations and the Rayleigh-Ritz method of different orders are compared in Table 5 with and without considering the rotational inertia. Fig. 8 compares the corresponding eigenmodes considering the rotational inertia. Results showed that the Rayleigh Ritz method with 5th order and 6th order polynomials predicts virtually the same natural frequencies and eigenmodes of the first 3 modes, which matches well with USFOS results, and the difference is within 5%. The 4th order Rayleigh Ritz method predicts less accuracy for the 3rd eigenmode. Even higher eigenmodes than the 3rd order are also calculated but are not shown. They can be readily obtained if needed.

Fig. 9 compares the first 3 eigenmodes using USFOS simulations with and without considering the rotational inertia. Results show that the rotational inertia is almost negligible for the first eigenmode of the turbine while its influence is significant for high order eigenmodes. When the rotational inertia is neglected, the errors thus brought for natural frequencies of the 2nd and 3rd modes approach up to 100%. The corresponding eigenmodes also differ significantly, especially for the 3rd mode. The tower tip rotation for the 3rd mode is much reduced when the rotational inertia is considered. It is therefore crucial to include the rotational inertia when high order eigenmodes become important.

For floating offshore wind turbines, the floater can often be treated as a rigid body while the floater connection to the tower bottom may have a finite rotational stiffness k_{rot}. In a nondimensional format with respect to tower properties, the stiffness becomes $\eta_{rot} = \frac{k_{rot}L_T}{E_T I_{Tb}}$. Table 6 compares natural frequencies of the tapered turbine tower with different bottom connection stiffness using USFOS and the Rayleigh-Ritz method of 6th order. The rotational inertia at the tower tip J_{RNA} is considered. The corresponding eigenmodes are compared in Fig. 10. The Rayleigh-Ritz method of 6th order shows excellent prediction of the first three natural frequencies and eigenmodes for the tapered turbine tower with finite bottom stiffness, and the error is within 5%. With a smaller bottom stiffness, the natural frequencies become lower, and the tower tends to become more flexible to lateral deflection.

3.4. High order natural frequencies and eigenmodes for monopile supported offshore wind turbines

High order natural frequencies and eigenmodes for a monopile supported offshore wind turbine with a tapered tower are considered, see Fig. 11. The foundation stiffness is modelled as a set of cross coupled translational and rotational springs at the mudline as described in Section 2.2.

Using the Rayleigh-Ritz method, a complete 6th order polynomial is adopted for the tapered tower as in section 3.3. One main difference is that the term $\varphi_0 = 1$ needs to be included since the tower base deflection is no longer zero. A 4th order polynomial is used for the monopile including the term $\varphi_0 = 1$ for non-zero monopile lateral displacement at the mudline. The corresponding trial functions are as follows:

$$\frac{w_{tower}(z_1)}{L_T} = a_0 \cdot 1 + a_1\left(\frac{z_1}{L_T}\right) + a_2\left(\frac{z_1}{L_T}\right)^2 + a_3\left(\frac{z_1}{L_T}\right)^3 + a_4\left(\frac{z_1}{L_T}\right)^4 + a_5\left(\frac{z_1}{L_T}\right)^5 + a_6\left(\frac{z_1}{L_T}\right)^6 \quad 0 \leq \frac{z_1}{L_T} \leq 1 \tag{17}$$

$$\frac{w_{mono}(z_2)}{L_T} = g_0 \cdot 1 + g_1\left(\frac{z_2}{L_T}\right) + g_2\left(\frac{z_2}{L_T}\right)^2 + g_3\left(\frac{z_2}{L_T}\right)^3 + g_4\left(\frac{z_2}{L_T}\right)^4 \quad 0 \leq \frac{z_2}{L_T} \leq \gamma = \frac{L_S}{L_T} \tag{18}$$

where z_1 and z_2 are the vertical coordinate of the tower and monopile in the local coordinate system as defined in Fig. 11, respectively. $w_{tower}(z_1)$ and $w_{mono}(z_2)$ are the lateral deflections of the tower and the monopile, which are nondimensionalized with respect to the tower height L_T. $\gamma = L_S/L_T$ is the ratio of the monopile height above the mudline L_S over the tower height L_T.

At the connection of the tower bottom and the monopile, there is a significant change of cross section diameter and thickness. The following continuity and compatibility requirements in Eq. (19) shall be satisfied at the connection, which ensure that lateral
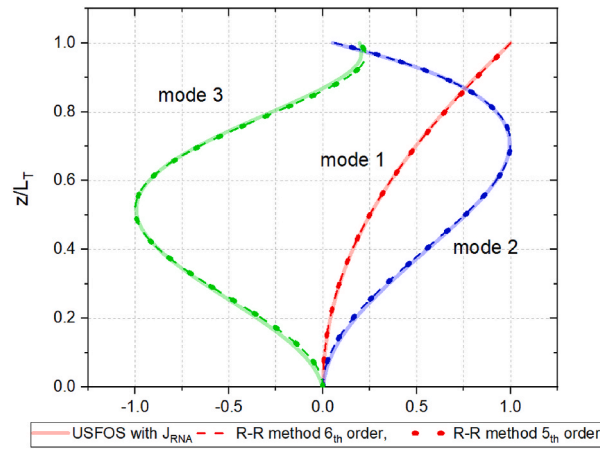
Fig. 8. First three eigenmodes of the DTU 10 MW turbine tower considering varying tower cross sections and a rigid base.
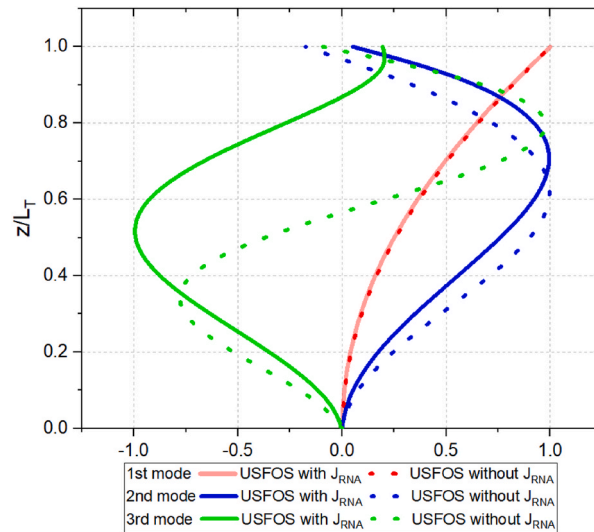

Fig. 9. USFOS simulations for the first three eigenmodes of the DTU 10 MW turbine tower with and without the rotational inertia.

Table 6
Natural frequencies [HZ] of the DTU 10 MW reference turbine tower with different rotational stiffnesses.

| Mode (Hz)	USFOS $\eta_{rot} = 1$	R–R method, 6th order $\eta_{rot} = 1$	Error	USFOS $\eta_{rot} = 10$	R–R method, 6th order $\eta_{rot} = 10$	Error
1st mode	0.163	0.164	0.6%	0.258	0.257	−0.4%
2nd mode	1.175	1.164	−0.9%	1.366	1.361	−0.4%
3rd mode	2.728	2.782	2.0%	3.170	3.274	3.3%
Mode (Hz)	USFOS $\eta_{rot} = 100$	R–R method, 6th order $\eta_{rot} = 100$	Error	USFOS $\eta_{rot} = inf$	USFOS $\eta_{rot} = inf$	Error
1st mode	0.279	0.278	−0.4%	0.282	0.281	−0.4%
2nd mode	1.435	1.432	−0.2%	1.444	1.441	−0.2%
3rd mode	3.445	3.586	4.1%	3.490	3.639	4.3%
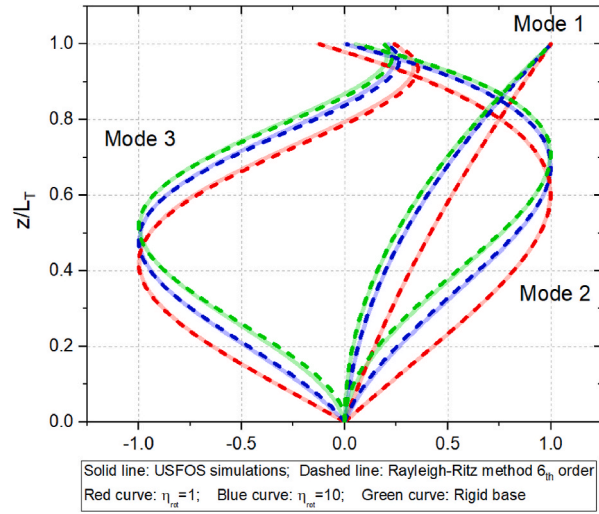
Fig. 10. First three eigenmodes of the DTU 10 MW turbine tower considering varying tower cross sections and finite rotational stiffnesses at the base.
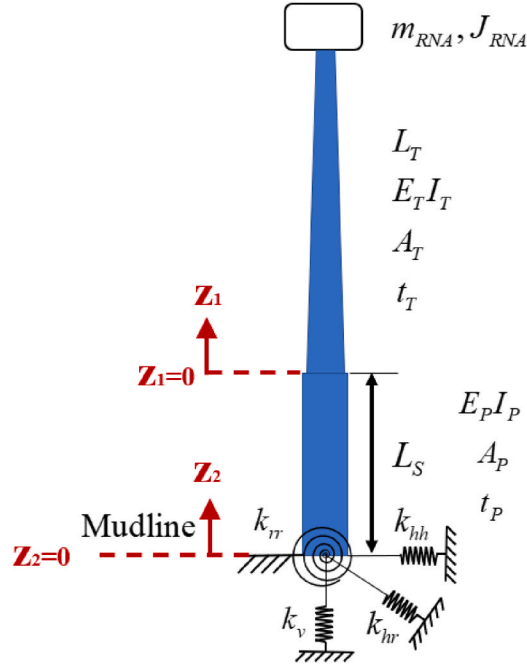

Fig. 11. A simplified model for monopile supported offshore wind turbines with tapered towers and cross coupled springs as foundation stiffness.

displacements and slopes are continuous over the cross-section dimension changes, and common bending moments and shear forces are carried at the intersection.

$$
\begin{cases}
\text{Disp continuity} : w_{tower}(z_1 = 0) = w_{mono}(z_2 = \gamma L_T) \\
\text{Slope continuity} : w'_{tower}(z_1 = 0) = w'_{mono}(z_2 = \gamma L_T) \\
\text{Moment} : -E_T I_T w''_{tower}(z_1 = 0) = -E_P I_P w''_{mono}(z_2 = \gamma L_T) \\
\text{Shear} : -E_T I_T w'''_{tower}(z_1 = 0) = -E_P I_P w'''_{mono}(z_2 = \gamma L_T)
\end{cases}
\tag{19}
$$

From Eq. (19), the following relationship can be established between the shape function coefficients of the tower and the monopile:

$$\begin{bmatrix} a_0 \\ a_1 \\ a_2 \\ a_3 \end{bmatrix} = \begin{bmatrix} 1 & \gamma & \gamma^2 & \gamma^3 & \gamma^4 \\ 0 & 1 & 2\gamma & 3\gamma^2 & 4\gamma^3 \\ 0 & 0 & \dfrac{E_P I_P}{E_T I_T} & \dfrac{E_P I_P}{E_T I_T}3\gamma & \dfrac{E_P I_P}{E_T I_T}6\gamma^2 \\ 0 & 0 & 0 & \dfrac{E_P I_P}{E_T I_T} & \dfrac{E_P I_P}{E_T I_T}4\gamma \end{bmatrix} \begin{bmatrix} g_0 \\ g_1 \\ g_2 \\ g_3 \\ g_4 \end{bmatrix} = \mathbf{A} \cdot \mathbf{g} \tag{20}$$

$\mathbf{A}_{4\times5}$ is the connectivity matrix. The transformation matrix $\mathbf{T}_{5\times7}$ between the vector for the monopile shape function coefficients $\mathbf{g}_{5\times1}$ and that for the tower $\mathbf{a}_{7\times1}$ is therefore expressed as:

$$\begin{bmatrix} g_0 \\ g_1 \\ g_2 \\ g_3 \\ g_4 \end{bmatrix} = \left[(\mathbf{A}^{-1})_{5\times4}, \mathbf{0}_{5\times3} \right] \begin{bmatrix} a_0 \\ a_1 \\ a_2 \\ a_3 \\ a_4 \\ a_5 \\ a_6 \end{bmatrix} = \mathbf{T}_{5\times7} \cdot \mathbf{a}_{7\times1} \tag{21}$$

where $(\mathbf{A}^{-1})_{5\times4}$ is the Moore-Penrose inverse or the generalized inverse of the non-square matrix $\mathbf{A}$. The Moore Penrose inverse matrix exists and is unique when $\mathbf{A}$ matrix is in full rank.

With the established trial functions for the lateral deflection of the monopile and the tower, the maximum strain energy $U_{\max}$ and the kinetic energy T_0 can be formulated. Following Eq. (6), the mass matrix $\mathbf{M}$ and the stiffness matrix $\mathbf{K}$ for a monopile turbine with a tapered tower and three coupled springs as foundation stiffnesses can be expressed as:

$$M_{ij} = \underbrace{\int_0^{\gamma L_T} \rho_P A_P T_{pi} \varphi_{p-1}(x)\varphi_{q-1}(x)T_{qj}dx}_{Monopile} + \underbrace{\int_0^{L_T} \rho_T A_T(z)\varphi_{i-1}(z)\varphi_{j-1}(z)dz}_{Tower}$$

$$+\underbrace{m_{RNA}\varphi_{i-1}(L_T)\varphi_{j-1}(L_T)}_{RNA\ mass} + \underbrace{\left[J_{RNA}\frac{d\varphi_{i-1}(z)}{dz}\frac{d\varphi_{j-1}(z)}{dz} \right]_{z=L_T}}_{RNA\ rotational\ inertia}; \tag{22}$$

$$i,j \in [1,2,3,\cdots,7], p,q \in [1,2,3,4,5];$$

$$K_{ij} = \underbrace{\int_0^{\gamma L_T} E_P I_P T_{pi}\frac{d^2\varphi_{p-1}(z_2)}{dz_2{}^2}\frac{d^2\varphi_{q-1}(z_2)}{dz_2{}^2}T_{qj}dz}_{Monopile} + \underbrace{\int_0^{L_T} E_T I_T(z)\frac{d^2\varphi_{i-1}(z_1)}{dz_1{}^2}\frac{d^2\varphi_{j-1}(z_1)}{dz_1{}^2}dz_1}_{Tower}$$

$$+\underbrace{\left[k_{hh}T_{pi}\varphi_{p-1}(z_2)\varphi_{q-1}(z_2)T_{qj} + k_{rr}T_{pi}\frac{d\varphi_{p-1}(z_2)}{dz_2}\frac{d\varphi_{q-1}(z_2)}{dz_2}T_{qj} + 2k_{hr}T_{pi}\varphi_{p-1}(z_2)\frac{d\varphi_{q-1}(z_2)}{dz_2}T_{qj} \right]_{z_2=0}}_{Foundation\ springs} \tag{23}$$

$$i,j \in [1,2,3,\cdots,7], p,q \in [1,2,3,4,5];$$

where the expressions follow the Einstein summation convention. The final expressions for the mass and stiffness matrices are given in Appendix C, from which nondimensional parameters that govern the natural frequencies and eigenmodes of monopile supported offshore turbines are summarized in Table 7.

The modified DTU 10 MW wind turbine tower mounted on a monopile is adopted for further illustration and is analyzed in USFOS. The turbine tower properties are given in Table 4. The monopile length above the mudline is $L_S = 40\ m$ and the pile penetrates $L_P = 42$

Table 7
Governing nondimensional parameters for monopile offshore wind turbines.

Dimensionless parameter	Formula	Dimensionless parameter	Formula
Length ratio γ	$\gamma = \dfrac{L_S}{L_T}$	Non-dimensional tower bending stiffness	$\dfrac{E_T I_{Tb}}{\rho_T A_{Tb} L_T{}^4}$
Mass ratio α	$\alpha = \dfrac{m_{RNA}}{\rho_T A_{Tb} L_T}$	Non-dimensional foundation lateral stiffness η_{hh}	$\eta_{hh} = \dfrac{k_{hh}L_T^3}{E_T I_{Tb}}$
Non-dimensional rotational inertia	$\beta = \dfrac{J_{RNA}}{\rho_T A_{Tb} L_T{}^3}$	Non-dimensional foundation cross stiffness η_{hr}	$\eta_{hr} = \dfrac{k_{hr}L_T^2}{E_T I_{Tb}}$
Mass density ratio of pile over tower bottom	$\dfrac{\rho_P A_P}{\rho_T A_{Tb}}$	Non-dimensional foundation rotational stiffness η_{rr}	$\eta_{rr} = \dfrac{k_{rr}L_T}{E_T I_{Tb}}$
Bending stiffness ratio	$\dfrac{E_P I_P}{E_T I_{Tb}}$		

m into the soil. The monopile has a diameter of $D_P = 9\ m$ and a thickness of $t_P = 110$ mm [30].

The monopile is considered fixed at the mudline in the first place. Natural frequencies predicted by the Rayleigh-Ritz method and USFOS simulations are compared with in Table 8 for the first three modes, and the corresponding eigenmodes are plotted in Fig. 12. The predicted natural frequencies and eigenmodes show excellent agreement.

Next, the soil-pile interaction is modelled as three coupled springs as shown in Fig. 11, and the foundation stiffness values suggested by Shadlou and Bhattacharya [16] in Table 1 are used. The soil conditions are considered simply to be homogeneous with constant soil stiffness along the embedded depth. The Young's modulus of soil E_{so} is crucial in determining the foundation stiffness. Two soil Young's modulus are selected, i.e., $E_{so} = 30$ Mpa, which is representative of the Siemens 3.6 MW at the Walney 1 site [16] and $E_{so} = 5$ Mpa as a kind of soft soil. The calculated foundation stiffnesses for the coupled springs are given in Table 9. In USFOS modelling, the boundary of the monopile bottom is represented as coupled springs with the same values as given in Table 9. Natural frequencies using the Rayleigh-Ritz method and USFOS simulations are compared in Table 10 for the first three modes, and the corresponding eigenmodes are plotted in Fig. 13. The predicted natural frequencies and eigenmodes again show excellent agreement, demonstrating high fidelity of the approach. From Fig. 13, the mudline displacement is generally small for the primary eigenmode and become evident for the 2nd and 3rd modes, especially with the soft soil condition. This is the case also for monopile rotations at the mudline.

4. Modelling of soil-monopile interactions

So far, the agreement between numerical simulations and the analytical method is excellent. The problem that remains is how well the coupled spring model represents real soil flexibilities. In addition, by assuming coupled springs, the inertia effects and kinetic energy carried by the pile underneath the mudline are disregarded. These effects will be explored in this section, where soil conditions are explicitly modelled using USFOS.

4.1. USFOS modelling of monopile foundation

USFOS is originally a tool tailored for jacket structures, where the foundation normally consists of a series of slender piles connected to the legs. Each single pile experiences axial resistance (T-Z and Q-Z) and horizontal resistance (P-Y) as recommended in API-RPGEO [14] and DNV-ST-0126 [15]. The large distance between the piles provides the global bending resistance of the jackets. In USFOS [36], it is stated that if a jacket pile model is used to represent large diameter monopiles, the global bending resistance will be underestimated. This is mainly due to the large dimensions of monopiles with a much larger friction area, which provides an additional bending resistance compared to the smaller piles used for jackets.

Recently, a monopile element for large diameter piles was established in USFOS [36] by subdividing the pile into a limited number (8 or 16 often used) of "integration points" or "auxiliary piles", refer Fig. 14. Each represents a certain arc of the monopile. Forces occurring in each single pile is transferred to the monopile, and the monopile resistance is obtained by summing up contributions from all auxiliary piles along the monopile circumference including the shear contribution.

4.2. Homogenous soil conditions

The DTU 10 MW turbine on a monopile foundation continues 42 m into the soil following the design of Bachynski and Ormberg [30]. The monopile has a diameter of 9 m and a thickness of 11 cm. The soil condition is considered homogenous in the first place. Two soil stiffnesses of 33.5 MN/m/m and 100 MN/m/m, i.e. (Force/unit lateral deflection/unit pile length) are assumed for the P-y curves, representing relatively soft and stiff soils. The established monopile turbine model is shown in Fig. 15. The blades are equipped with high stiffness (rigid) materials so that the effects of blade flexibilities are disregarded.

In order to enable a fair comparison, the homogenous soil stiffness needs to be transformed into an equivalent set of coupled springs at the mudline. From the literature, two expressions are found useful assuming flexible pile behavior. Poulos and Davis [24] suggested the following spring stiffness for homogenous soil conditions:

$$\begin{bmatrix} F \\ M \end{bmatrix} = \begin{bmatrix} \dfrac{k_{sub}D_p}{\beta_{\text{pile}}} & -\dfrac{k_{sub}D_p}{2\beta_{\text{pile}}^2} \\ -\dfrac{k_{sub}D_p}{2\beta_{\text{pile}}^2} & \dfrac{k_{sub}D_p}{2\beta_{\text{pile}}^3} \end{bmatrix} \begin{bmatrix} \rho \\ \theta \end{bmatrix}$$

(24)

where $\beta_{\text{pile}} = \sqrt[4]{\dfrac{k_{sub}D_p}{4E_P L_P}}$ is a characteristic pile slenderness parameter.

Table 8

Natural frequencies [HZ] of the DTU 10 MW turbine tower supported on a monopile foundation fixed at the mudline.

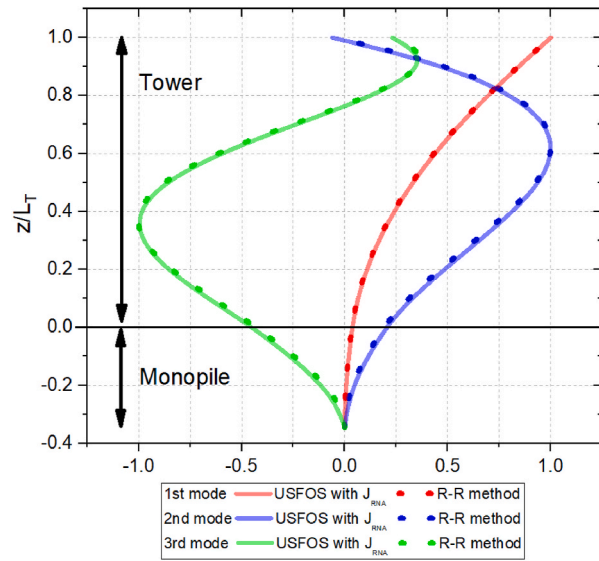| Mode (Hz)	USFOS with J_{RNA}	The Rayleigh-Ritz method	Error
1st mode	0.245	0.245	0.0%
2nd mode	1.249	1.250	0.1%
3rd mode	2.528	2.623	3.8%

Fig. 12. First three eigenmodes of the DTU 10 MW turbine tower mounted on a monopile foundation fixed at the mudline.

Table 9
Calculated foundation stiffnesses for the cross coupled springs.

	K_{hh} (GN/m)	K_{hr} (GN)	K_{rr} (GNm/rad)	η_{hh}	η_{hr}	η_{rr}
Rigid pile E_{so} = 30 MPa	2.25	−47.7	1700	1640	−301	92.8
Flexible pile E_{so} = 30 MPa	1.31	−18.7	469	957	−118	25.6
Rigid pile E_{so} = 5 MPa	0.374	−7.95	283	274	−50.2	15.5
Flexible pile E_{so} = 5 MPa	0.305	−7.64	289	223	−48.3	15.8

Table 10
Natural frequencies [HZ] of the DTU 10 MW turbine tower supported on a monopile foundation with cross coupled springs at the mudline.

Stiff soil	Foundation assuming flexibile pile E_{so} = 30 MPa			Foundation assuming rigid pile E_{so} = 30 MPa		
Mode (Hz)	USFOS	R–R method	error	USFOS	R–R method	error
1_{st} mode	0.214	0.214	0.0%	0.234	0.234	−0.0%
2_{nd} mode	0.995	0.996	0.1%	1.134	1.136	0.2%
3_{rd} mode	1.898	1.919	1.2%	2.096	2.141	2.1%
Soft soil	Foundation assuming flexibile pile E_{so} = 5 MPa			Foundation assuming rigid pile E_{so} = 5 MPa		
Mode (Hz)	USFOS	R–R method	error	USFOS	R–R method	error
1_{st} mode	0.183	0.184	0.1%	0.192	0.192	0.0%
2_{nd} mode	0.789	0.788	0.2%	0.840	0.840	0.0%
3_{rd} mode	1.669	1.672	0.2%	1.712	1.718	0.3%

Psaroudakis et al. [38] derived an analytical solution for pile responses assuming the Winkler type spring on foundations. The following expressions were obtained for homogenous soil conditions:

$$
\begin{bmatrix} F \\ M \end{bmatrix} = \begin{bmatrix} 4E_p I_P \beta_{\text{pile}}^3 \dfrac{\sin(2\beta_{\text{pile}}L_P) + \sinh(2\beta_{\text{pile}}L_P)}{2 + \cos(2\beta_{\text{pile}}L_P) + \cosh(2\beta_{\text{pile}}L_P)} - 2E_p I_P \beta_{\text{pile}}^2 \dfrac{-\cos(2\beta_{\text{pile}}L_P) + \cosh(2\beta_{\text{pile}}L_P)}{2 + \cos(2\beta_{\text{pile}}L_P) + \cosh(2\beta_{\text{pile}}L_P)} \\ -2E_p I_P \beta_{\text{pile}}^2 \dfrac{-\cos(2\beta_{\text{pile}}L_P) + \cosh(2\beta_{\text{pile}}L_P)}{2 + \cos(2\beta_{\text{pile}}L_P) + \cosh(2\beta_{\text{pile}}L_P)} \quad 2E_p I_P \beta_{\text{pile}} \dfrac{-\sin(2\beta_{\text{pile}}L_P) + \sinh(2\beta_{\text{pile}}L_P)}{2 + \cos(2\beta_{\text{pile}}L_P) + \cosh(2\beta_{\text{pile}}L_P)} \end{bmatrix} \begin{bmatrix} \rho \\ \theta \end{bmatrix} \tag{25}
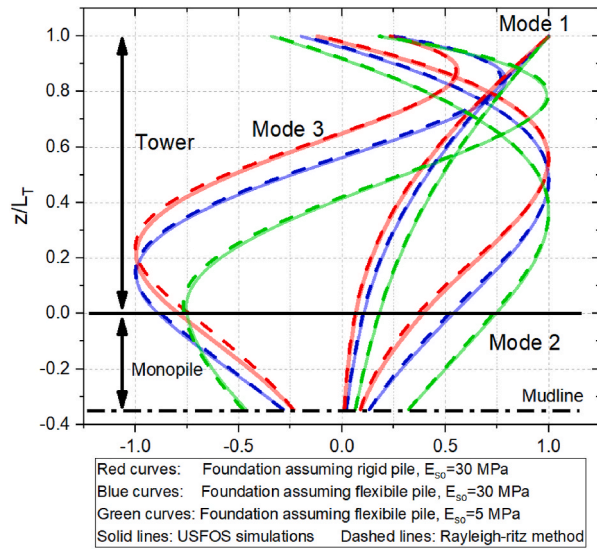$$

Fig. 13. First three eigenmodes of the DTU 10 MW turbine tower mounted on a monopile foundation with cross coupled springs at the mudline.
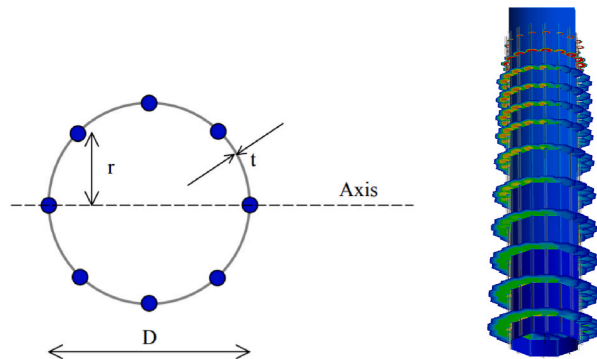

Fig. 14. (Left) Pipe with 8 integration points along the circumference [37]; (right) The disk model of soil springs in USFOS. Each disk represents a soil layer and the size of the disk is proportional to the soil stiffness.

Table 11 compares natural frequencies of the first 3 modes using USFOS simulations and the Rayleigh-Ritz solutions. The corresponding eigenmodes are plotted in Fig. 16. Results transpire that the Rayleigh-Ritz method based on Psaroudakis et al. [38]'s coupled-spring soil expressions yields an excellent match with USFOS simulations using *P-y* curves only. This is the case for both natural frequencies and eigenmodes. The Rayleigh-Ritz method with Poulos and Davis [24]'s formulae shows less agreement, but is still reasonably accurate. The formulations derived by Psaroudakis et al. [38] are therefore highly recommended.

The good agreement shows that the coupled spring model represents realistic soil conditions well if the coupled spring stiffnesses are properly selected and calculated. Neglecting the inertia effects of embedded piles does not seem to influence much the obtained eigenmodes, even for high order eigenmodes. It is also interesting to find from Fig. 16 that evidently there exists a pivot point for the embedded piles, where the pile lateral displacement vanishes. The position of the pivot point depends on soil stiffness distribution over the embedded depth.

The above USFOS simulations considered only lateral stiffness with *P-y* curves. In practice, the shear resistance (*T-z*) can also contribute to resisting lateral bending moment for large diameter monopiles. By introducing additionally *T-z* curves (assuming the same stiffness as the *P-y* curves) and *Q-z* curves for shear resistance in simulations, the natural frequencies obtained with USFOS are given in Table 11. The shear effects do not show a significant influence on the natural frequencies.

4.3. Site measured soil condition

Soil is a heterogeneous material with properties that vary vertically and horizontally, see e.g., layered soils in Fig. 17(left). The inherent variability of soil properties is due to the natural heterogeneity resulting from continuous geological processes [39]. In this section, quantitative values obtained from measurement campaigns at Dogger Bank are used as a basis for the *P-y* curves. The soil

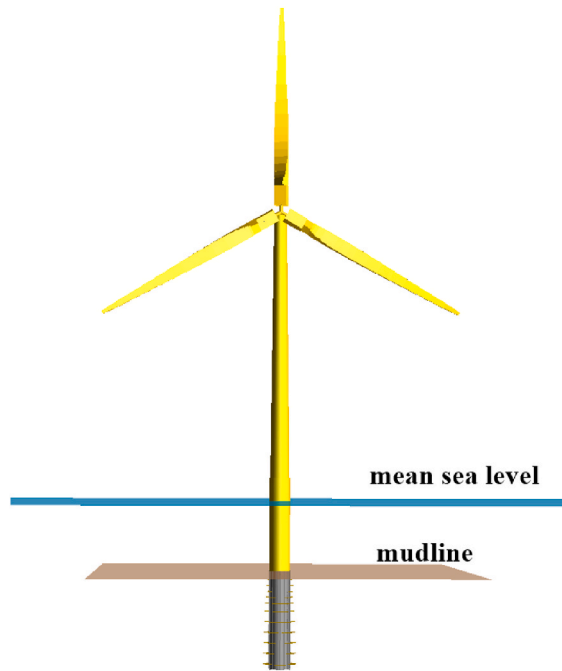**Fig. 15.** USFOS modelling of the monopile supported DTU 10 MW turbine with soil foundations.

Table 11
Natural frequencies [HZ] of the DTU 10 MW turbine tower supported on a monopile foundation with homogenous soil stiffnesses.

Soil stiffness	Mode (Hz)	USFOS with P-y curves only	R–R method based on Psaroudakis et al. [38] soil	R–R method based on Poulos and Davis [24] soil	USFOS with P-y, T-z and Q-z curves
$k_s = k_{sub}D_P =$ 33.5$MN/m/m$	1$_{st}$ mode	0.201	0.201	0.215	0.203
	2$_{nd}$ mode	0.914	0.919	1.001	0.923
	3$_{rd}$ mode	1.802	1.825	1.912	1.812
$k_s = k_{sub}D_P =$ 100$MN/m/m$	1$_{st}$ mode	0.220	0.220	0.222	0.221
	2$_{nd}$ mode	1.041	1.046	1.068	1.049
	3$_{rd}$ mode	1.969	2.008	2.049	1.980

profile at the design location consists of a surface layer of dense sand (2 m) with underlying layers of stiff clays as reported in Horn [40]. Due to the stochastic nature of the measured soil properties, Horn [40] reported upper and lower estimates of the clay shear strength with linear fits. Based on the measured soil properties, nonlinear P-y curves were calculated based on the API-RPGEO [41] formulations and are modelled as elastic-plastic disks in USFOS. The corresponding initial tangential stiffnesses of the nonlinear P-y curves over the embedded depth are plotted in Fig. 17(right).

It is however difficult to find analytical formulations to determine the coupled spring stiffnesses for such complicated soil stiffness distributions. A possible approach is to find an equivalent homogenous soil stiffness and then use the formulations by Psaroudakis et al. [38] in Eq. (15). We selected two different ways of obtaining the equivalent constant soil stiffness. The first is to use a uniformly weighed average, which gives an equivalent stiffness of 66.4 MN/m/m. The second is to adopt a linearly weighed average by assuming a pivot point at half of the embedded depth, i.e., 0.5L$_P$. This yields an equivalent stiffness of 59.8 MN/m/m.

Table 12 compares natural frequencies of the first 3 modes using USFOS simulations and the Rayleigh-Ritz solutions with two different equivalent constant stiffness approximations. The corresponding eigenmodes are plotted in Fig. 18. The results show that the equivalent constant stiffnesses approximated by both methods give reasonably good estimation. The linearly weighed approach assuming a pivot point at 0.5L$_P$ shows better accuracy. From USFOS simulations in Fig. 18, the true pivot point is approximately 2/3 L$_P$ below the mudline. It is expected that the linearly weighed approach assuming a pivot point at the exact position will give even better agreement.
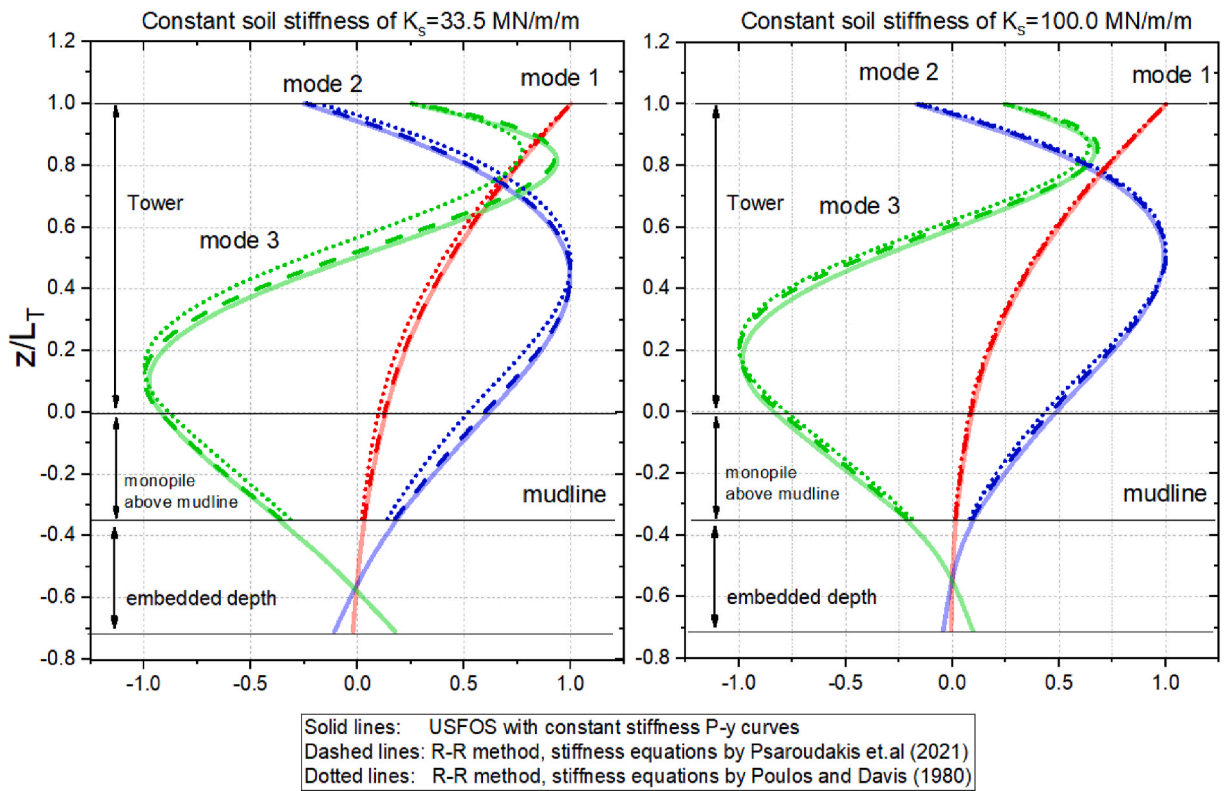
Solid lines: USFOS with constant stiffness P-y curves
Dashed lines: R-R method, stiffness equations by Psaroudakis et.al (2021)
Dotted lines: R-R method, stiffness equations by Poulos and Davis (1980)

Fig. 16. First three eigenmodes of monopile supported DTU 10 MW turbines with homogenous soil foundations of different stiffnesses.
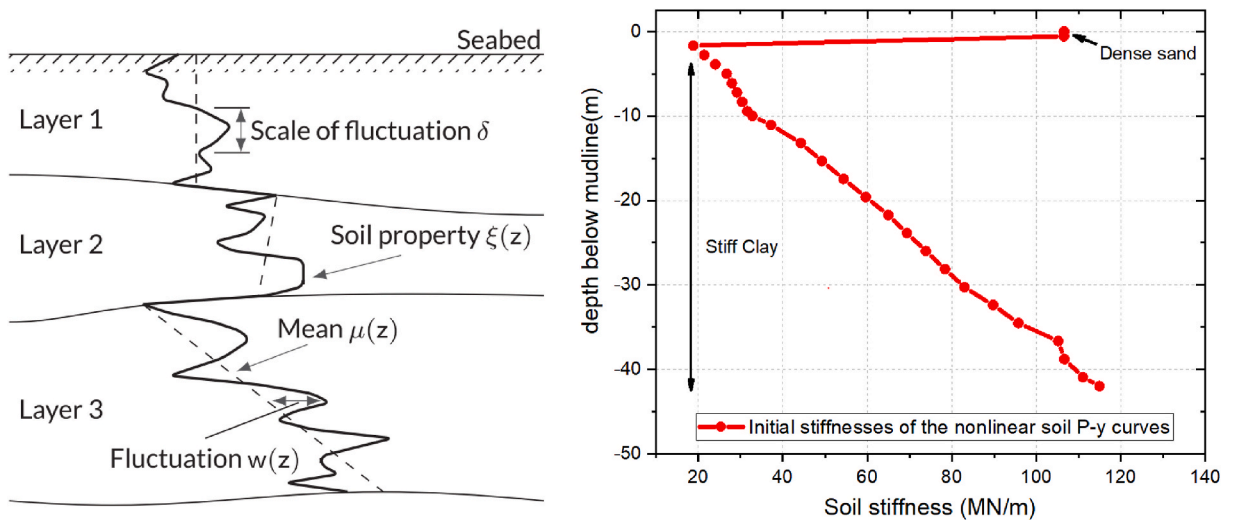

Fig. 17. (Left) Illustrative drawing of a random field soil model from Smilden, Sørum [39] (right) Initial tangential stiffness of the nonlinear soil P-y curves at a Dogger Bank wind farm along the embedded depth used in Horn [40].

5. Discussions

The excellent agreement of the Rayleigh-Ritz solutions with the analytical and USFOS numerical simulations show high accuracy of the approach. The method is presented in matrix form in the appendices and can, together with the Duhamel's integral, be readily implemented in the buckling and collapse analysis and design of monopile supported offshore wind turbines according to the principles of Ultimate Limit States (ULS) and Accidental Limit States (ALS). In addition, the high accuracy of the predicted primary natural

Table 12

Natural frequencies (Hz) of the DTU 10 MW turbine tower supported on a monopile foundation with site measured soil stiffnesses.

Mode (Hz)	USFOS	R–R method with uniformly weighed soil stiffness	R–R method with linearly weighed stiffness
1_{st} mode	0.213	0.215	0.213
2_{nd} mode	0.977	1.007	0.995
3_{rd} mode	1.859	1.940	1.920
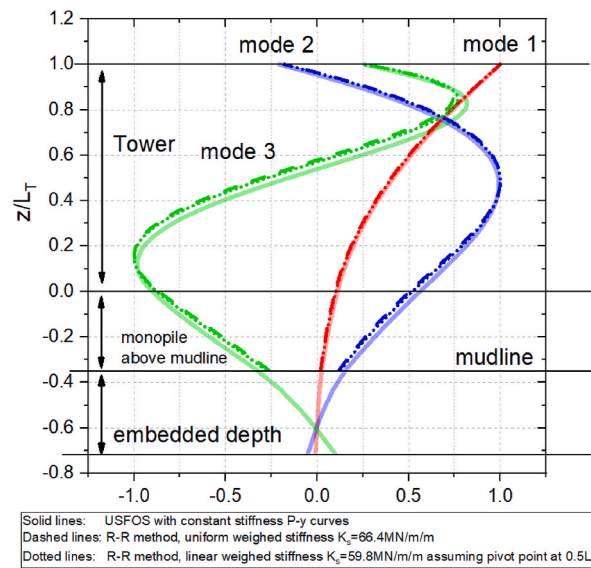
Fig. 18. First three eigenmodes of monopile supported DTU 10 MW turbines with site measure soil conditions.
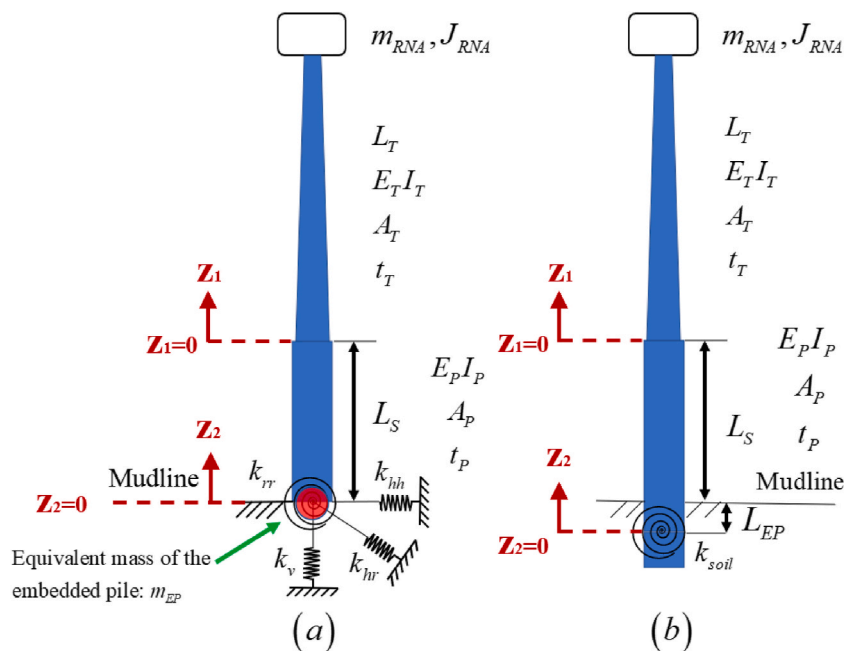
Fig. 19. (A) An equivalent mass of the embedded pile added to the cross coupled spring model to account for pile inertia effects. (b) The hinge-stiffness model for monopile supported offshore wind turbines.

frequency makes it a useful design tool to help avoid resonance from external excitation loads and to reduce resonance related fatigue effects in Fatigue Limit States (FLS).

The coupled spring model shows good accuracy for homogenous soil conditions and for realistic site measured soil conditions. The effect of neglecting inertia forces and kinetic energy of the embedded pile is limited as regards primary and high order natural frequencies and eigenmodes. This seems to contradict the conclusion drawn in Bir and Jonkman [18], where it is stated that when higher modes play a role in turbine dynamics, the coupled spring representation of soil could lead to erroneous results. This may be due to the different formulae used for the coupled spring stiffnesses. In case the inertia effects of embedded piles become important, it is convenient to modify the present coupled spring model by introducing an equivalent mass at the mudline m_{EP}, representing the mass of the embedded pile, see Fig. 19(a). m_{EP} may be determined in the same way as the equivalent tower mass in Eq. (1). This will give an extra term in Eq. (22) and therefore in the resulting mass matrix.

Another approach is to introduce a new foundation model as shown in Fig. 19(b), termed hinge-stiffness (HS) foundation. The foundation is modelled as a pile with an effective length of L_{EP}, the bottom of which is at the pile pivot point with zero lateral displacement. This method includes partly the inertia effects of embedded piles. Without lateral displacements at the base, the soil stiffness can be simplified into only one rotational stiffness k_{soil}. The model is inspired from direct observation of USFOS simulation results, where a pivot point clearly exists for the embedded pile. It will be straightforward to modify the Rayleigh-Ritz expressions in Section 3.4 to account for the hinge-stiffness foundation form. The remaining problem is how to determine the effective embedded pile length L_{EP} and the rotational stiffness k_{soil}. The effective embedded pile length can be found by force and moment equilibrium assuming certain soil stiffness distributions. When homogenous soil stiffness is assumed, moment equilibrium yields an effective length of $\frac{1}{2}L_P$. Darvishi-Alamouti, Bahaari [42] derived that the effective length would be between $\frac{2}{3}L_P$ and $\frac{3}{4}L_P$ if a linear distribution of soil stiffness is assumed along the depth. This is consistent with observations from USFOS simulations. The foundation stiffness k_{soil} can be readily determined for a given pivot point location and soil stiffness distributions. In addition, it may be useful to transform existing formulae for the cross coupled spring stiffnesses directly into the present hinge-stiffness foundation model without significant efforts. This is not explored further as the coupled spring model worked very well and the formulations for the spring stiffnesses are already well established.

6. Conclusions

This paper derived a Rayleigh-Ritz solution for high order natural frequencies and eigenmodes of monopile supported offshore wind turbines considering explicitly the tapered towers and soil pile interactions. The model is applied to the DTU 10 MW turbine mounted on a monopile foundation with different soil conditions. The predicted results are compared with nonlinear finite element USFOS simulations. The following conclusions are drawn.

(1) The proposed Rayleigh-Ritz solution is capable of predicting high order natural frequencies and eigenmodes of monopile offshore wind turbines with very high accuracy. The solution is formulated on the matrix form and can be readily utilized in the FLS, ULS and ALS analysis and design of offshore wind turbines.
(2) The coupled spring model represents well soil pile interactions for different soil conditions if the spring stiffnesses are calculated properly. The neglect of inertia effects and kinetic energy carried by the embedded pile has limited influence on the accuracy of the first 3 modes. The stiffness formulations by Psaroudakis, Mylonakis [38] are recommended for homogenous soil conditions.
(3) Direct observations of USFOS simulations indicate that a pivot point exists on the embedded pile, where the lateral displacement vanishes. A simplified hinge-stiffness foundation model with an effective embedded pile length and a rotational soil spring is proposed. The effective embedded length varies with the soil stiffness distributions over the embedded depth, and the pivot point is generally located in the lower half of the pile.

Declaration of competing interest

The authors declare that they have no known competing financial interests or personal relationships that could have appeared to influence the work reported in this paper.

Data availability

Data will be made available on request.

Acknowledgements

Appendix

High order natural frequencies and eigenmodes can be readily obtained by solving the matrix equation $(\mathbf{K} - \omega^2\mathbf{M})\mathbf{a} = \mathbf{0}$, and the mass and stiffness matrices are presented in the following for convenient implementation. The relevant MATLAB codes can be shared upon private communication with the authors.

A. Generalized stiffness and mass matrices for a uniform cantilever beam with a tip mass

The complete 4th order polynomial terms are recommended for a uniform cross section with a tip mass as follows. The φ_0 term vanishes with a rigid base.

$$\varphi_1 = \frac{z}{L}, \varphi_2 = \left(\frac{z}{L}\right)^2, \varphi_3 = \left(\frac{z}{L}\right)^3, \varphi_4 = \left(\frac{z}{L}\right)^4 \tag{A.1}$$

Let $\alpha = \frac{m_{RNA}}{mL}$ and $\beta = \frac{J_{RNA}}{mL^3}$, where m is the tower mass per unit length. The mass matrix $\mathbf{M}$ is expressed as:

$$\mathbf{M} = mL \left(\begin{bmatrix} 1/3 & 1/4 & 1/5 & 1/6 \\ 1/4 & 1/5 & 1/6 & 1/7 \\ 1/5 & 1/6 & 1/7 & 1/8 \\ 1/6 & 1/7 & 1/8 & 1/9 \end{bmatrix} + \alpha \begin{bmatrix} 1 & 1 & 1 & 1 \\ 1 & 1 & 1 & 1 \\ 1 & 1 & 1 & 1 \\ 1 & 1 & 1 & 1 \end{bmatrix} + \beta \begin{bmatrix} 1 & 2 & 3 & 4 \\ 2 & 4 & 6 & 8 \\ 3 & 6 & 9 & 12 \\ 4 & 8 & 12 & 16 \end{bmatrix} \right) \tag{A.2}$$

$\qquad$ beam $\quad$ tip mass $\quad$ tip rotation

The stiffness matrix $\mathbf{K}$ becomes

$$\mathbf{K} = \frac{EI}{L^3} \begin{bmatrix} 0 & 0 & 0 & 0 \\ 0 & 4 & 6 & 8 \\ 0 & 6 & 12 & 18 \\ 0 & 8 & 18 & \frac{144}{5} \end{bmatrix} \tag{A.3}$$

B. Generalized stiffness and mass matrices for a tapered turbine tower

The complete 6th order polynomial terms are recommended for a tapered turbine tower as follows. The φ_0 term vanishes at the tower base with finite rotational stiffness only.

$$\varphi_1 = \frac{z}{L_T}, \varphi_2 = \left(\frac{z}{L_T}\right)^2, \varphi_3 = \left(\frac{z}{L_T}\right)^3, \varphi_4 = \left(\frac{z}{L_T}\right)^4, \varphi_5 = \left(\frac{z}{L_T}\right)^5, \varphi_6 = \left(\frac{z}{L_T}\right)^6 \tag{B.1}$$

Let $\alpha = \frac{m_{RNA}}{\rho_T A_{Tb} L_T}$ and $\beta = \frac{J_{RNA}}{\rho_T A_{Tb} L_T^3}$, where ρ_T is the density of the tower material and A_{Tb} is the cross-section area at the tower base. The mass matrix $\mathbf{M}$ is expressed as:

$$\mathbf{M} =$$

$$\rho_T A_{Tb} L_T \left(\begin{bmatrix} (1/3c_0 + 1/4c_1) & (1/4c_0 + 1/5c_1) & (1/5c_0 + 1/6c_1) & (1/6c_0 + 1/7c_1) & (1/7c_0 + 1/8c_1) & (1/8c_0 + 1/9c_1) \\ (1/4c_0 + 1/5c_1) & (1/5c_0 + 1/6c_1) & (1/6c_0 + 1/7c_1) & (1/7c_0 + 1/8c_1) & (1/8c_0 + 1/9c_1) & (1/9c_0 + 1/10c_1) \\ (1/5c_0 + 1/6c_1) & (1/6c_0 + 1/7c_1) & (1/7c_0 + 1/8c_1) & (1/8c_0 + 1/9c_1) & (1/9c_0 + 1/10c_1) & (1/10c_0 + 1/11c_1) \\ (1/6c_0 + 1/7c_1) & (1/7c_0 + 1/8c_1) & (1/8c_0 + 1/9c_1) & (1/9c_0 + 1/10c_1) & (1/10c_0 + 1/11c_1) & (1/11c_0 + 1/12c_1) \\ (1/7c_0 + 1/8c_1) & (1/8c_0 + 1/9c_1) & (1/9c_0 + 1/10c_1) & (1/10c_0 + 1/11c_1) & (1/11c_0 + 1/12c_1) & (1/12c_0 + 1/13c_1) \\ (1/8c_0 + 1/9c_1) & (1/9c_0 + 1/10c_1) & (1/10c_0 + 1/11c_1) & (1/11c_0 + 1/12c_1) & (1/12c_0 + 1/13c_1) & (1/13c_0 + 1/14c_1) \end{bmatrix} \right.$$

$$\left. + \alpha \begin{bmatrix} 1 & 1 & 1 & 1 & 1 & 1 \\ 1 & 1 & 1 & 1 & 1 & 1 \\ 1 & 1 & 1 & 1 & 1 & 1 \\ 1 & 1 & 1 & 1 & 1 & 1 \\ 1 & 1 & 1 & 1 & 1 & 1 \\ 1 & 1 & 1 & 1 & 1 & 1 \end{bmatrix} + \beta \begin{bmatrix} 1 & 2 & 3 & 4 & 5 & 6 \\ 2 & 4 & 6 & 8 & 10 & 12 \\ 3 & 6 & 9 & 12 & 15 & 18 \\ 4 & 8 & 12 & 16 & 20 & 24 \\ 5 & 10 & 15 & 20 & 25 & 30 \\ 6 & 12 & 18 & 24 & 30 & 36 \end{bmatrix} \right) \tag{B.2}$$

$$\mathbf{K}=$$

$$=\frac{E_T I_{Tb}}{L_T^3}\begin{bmatrix} 0 & 0 & 0 & 0 & 0 \\ 0 & (4b_0+2b_1+b_24/3) & (6b_0+4b_1+3b_2) & (8b_0+6b_1+24/5b_2) & (10b_0+8b_1+40/6b_2) & (12b_0+10b_1+60/7b_2) \\ 0 & (6b_0+4b_1+3b_2) & (12b_0+9b_1+36/5b_2) & (18b_0+72/5b_1+12b_2) & (24b_0+20b_1+120/7b_2) \\ & (30b_0+180/7b_1+180/8b_2) \\ 0 & (8b_0+6b_1+24/5b_2) & (18b_0+72/5b_1L+12b_2) & (144/5b_0+24b_1+144/7b_2) & (240/6b_0+240/7b_1+30b_2) \\ & (360/7b_0+360/8b_1+40b_2) \\ 0 & (10b_0+8b_1+40/6b_2) & (24b_0+20b_1+120/7b_2) & (240/6b_0+240/7b_1+30b_2) & (400/7b_0+50b_1+400/9b_2) \\ & (600/8b_0+600/9b_1+60b_2) \\ 0 & (12b_0+10b_1+60/7b_2) & (30b_0+180/7b_1+180/8b_2) & (360/7b_0+360/8b_1+40b_2) & (600/8b_0+600/9b_1+60b_2) \\ & (900/9b_0+90b_1+900/11b_2) \end{bmatrix}$$

$$+\frac{k_{rot}L_T}{E_T I_{Tb}}\begin{bmatrix} 1 & 0 & 0 & 0 & 0 & 0 \\ 0 & 0 & 0 & 0 & 0 & 0 \\ 0 & 0 & 0 & 0 & 0 & 0 \\ 0 & 0 & 0 & 0 & 0 & 0 \\ 0 & 0 & 0 & 0 & 0 & 0 \\ 0 & 0 & 0 & 0 & 0 & 0 \end{bmatrix}$$

(B.3)

C. Generalized stiffness and mass matrices for a monopile foundation offshore turbine considering tapered towers and soil-pile interactions

Let $\alpha=\frac{m_{RNA}}{\rho_T A_{Tb} L_T}, \beta=\frac{J_{RNA}}{\rho_T A_{Tb} L_T^3}$ and $\gamma=\frac{L_S}{L_T}$, where ρ_T is the density of tower material and A_{Tb} is the cross-section area at the tower base. For a monopile supported offshore turbine considering tapered towers and soil-pile interactions, the mass matrix $\mathbf{M}$ is expressed as:

$$\mathbf{M}_{7\times7}$$

$$
= \frac{\rho_P A_P}{\rho_T A_{Tb}} \mathbf{T}_{7\times5}^T
\begin{bmatrix}
\gamma & 1/2\gamma^2 & 1/3\gamma^3 & 1/4\gamma^4 & 1/5\gamma^5 \\
1/2\gamma^2 & 1/3\gamma^3 & 1/4\gamma^4 & 1/5\gamma^5 & 1/6\gamma^6 \\
1/3\gamma^3 & 1/4\gamma^4 & 1/5\gamma^5 & 1/6\gamma^6 & 1/7\gamma^7 \\
1/4\gamma^4 & 1/5\gamma^5 & 1/6\gamma^6 & 1/7\gamma^7 & 1/8\gamma^8 \\
1/5\gamma^5 & 1/6\gamma^6 & 1/7\gamma^7 & 1/8\gamma^8 & 1/9\gamma^9
\end{bmatrix}
\mathbf{T}_{5\times7} +
$$

$$
= \rho_T A_{Tb} L_T
\begin{bmatrix}
(1/1c_0+1/2c_1) & (1/2c_0+1/3c_1) & (1/3c_0+1/4c_1) & (1/4c_0+1/5c_1) & (1/5c_0+1/6c_1) & (1/6c_0+1/7c_1) & (1/7c_0+1/8c_1) \\
(1/2c_0+1/3c_1) & (1/3c_0+1/4c_1) & (1/4c_0+1/5c_1) & (1/5c_0+1/6c_1) & (1/6c_0+1/7c_1) & (1/7c_0+1/8c_1) & (1/8c_0+1/9c_1) \\
(1/3c_0+1/4c_1) & (1/4c_0+1/5c_1) & (1/5c_0+1/6c_1) & (1/6c_0+1/7c_1) & (1/7c_0+1/8c_1) & (1/8c_0+1/9c_1) & (1/9c_0+1/10c_1) \\
(1/4c_0+1/5c_1) & (1/5c_0+1/6c_1) & (1/6c_0+1/7c_1) & (1/7c_0+1/8c_1) & (1/8c_0+1/9c_1) & (1/9c_0+1/10c_1) & (1/10c_0+1/11c_1) \\
(1/5c_0+1/6c_1) & (1/6c_0+1/7c_1) & (1/7c_0+1/8c_1) & (1/8c_0+1/9c_1) & (1/9c_0+1/10c_1) & (1/10c_0+1/11c_1) & (1/11c_0+1/12c_1) \\
(1/6c_0+1/7c_1) & (1/7c_0+1/8c_1) & (1/8c_0+1/9c_1) & (1/9c_0+1/10c_1) & (1/10c_0+1/11c_1) & (1/11c_0+1/12c_1) & (1/12c_0+1/13c_1) \\
(1/7c_0+1/8c_1) & (1/8c_0+1/9c_1) & (1/9c_0+1/10c_1) & (1/10c_0+1/11c_1) & (1/11c_0+1/12c_1) & (1/12c_0+1/13c_1) & (1/13c_0+1/14c_1)
\end{bmatrix}
$$

$$
+\alpha
\begin{bmatrix}
1 & 1 & 1 & 1 & 1 & 1 & 1 \\
1 & 1 & 1 & 1 & 1 & 1 & 1 \\
1 & 1 & 1 & 1 & 1 & 1 & 1 \\
1 & 1 & 1 & 1 & 1 & 1 & 1 \\
1 & 1 & 1 & 1 & 1 & 1 & 1 \\
1 & 1 & 1 & 1 & 1 & 1 & 1 \\
1 & 1 & 1 & 1 & 1 & 1 & 1
\end{bmatrix}
+\beta
\begin{bmatrix}
0 & 0 & 0 & 0 & 0 & 0 & 0 \\
0 & 1 & 2 & 3 & 4 & 5 & 6 \\
0 & 2 & 4 & 6 & 8 & 10 & 12 \\
0 & 3 & 6 & 9 & 12 & 15 & 18 \\
0 & 4 & 8 & 12 & 16 & 20 & 24 \\
0 & 5 & 10 & 15 & 20 & 25 & 30 \\
0 & 6 & 12 & 18 & 24 & 30 & 36
\end{bmatrix}
$$

<div align="right">(C.1)</div>

$$\mathbf{K}_{7\times7} =$$

$$\frac{E_P I_P}{E_T I_{Tb}} \mathbf{T}_{7\times5}^T \begin{bmatrix} \dfrac{k_{hh}L_T^3}{E_P I_P} & \dfrac{k_{hr}L_T^2}{E_P I_P} & 0 & 0 & 0 \\[2mm] \dfrac{k_{rh}L_T^2}{E_P I_P} & \dfrac{k_{rr}L_T}{E_P I_P} & 0 & 0 & 0 \\[2mm] 0 & 0 & 4\gamma & 6\gamma^2 & 8\gamma^3 \\[2mm] 0 & 0 & 6\gamma^2 & 12\gamma^3 & 18\gamma^4 \\[2mm] 0 & 0 & 8\gamma^3 & 18\gamma^4 & \dfrac{144}{5}\gamma^5 \end{bmatrix} \mathbf{T}_{5\times7} +$$

$$\frac{E_T I_{Tb}}{L_T^3} \begin{bmatrix} 0 & 0 & 0 & 0 & 0 & 0 & 0 \\ 0 & 0 & 0 & 0 & 0 & 0 & 0 \\ 0 & 0 & (4b_0+2b_1+b_2 4/3) & (6b_0+4b_1+3b_2) & (8b_0+6b_1+24/5b_2) & (10b_0+8b_1+40/6b_2) & (12b_0+10b_1+60/7b_2) \\ 0 & 0 & (6b_0+4b_1+3b_2) & (12b_0+9b_1+36/5b_2) & (18b_0+72/5b_1+12b_2) & (24b_0+20b_1+120/7b_2) & \\ & & & & & & (30b_0+180/7b_1+180/8b_2) \\ 0 & 0 & (8b_0+6b_1+24/5b_2) & (18b_0+72/5b_1L+12b_2) & (144/5b_0+24b_1+144/7b_2) & (240/6b_0+240/7b_1+30b_2) & \\ & & & & & & (360/7b_0+360/8b_1+40b_2) \\ 0 & 0 & (10b_0+8b_1+40/6b_2) & (24b_0+20b_1+120/7b_2) & (240/6b_0+240/7b_1+30b_2) & (400/7b_0+50b_1+400/9b_2) & \\ & & & & & & (600/8b_0+600/9b_1+60b_2) \\ 0 & 0 & (12b_0+10b_1+60/7b_2) & (30b_0+180/7b_1+180/8b_2) & (360/7b_0+360/8b_1+40b_2) & & \\ & & (600/8b_0+600/9b_1+60b_2) & (900/9b_0+90b_1+900/11b_2) & & & \end{bmatrix}$$

(C.2)

References

[1] DNV-GL. Floating wind: THE POWER TO COMMERCIALIZE Insights and reasons for confidence. DNV report; 2020.

[2] Ramirez L, Fraile D, Brindley G. Offshore wind in Europe: key trends and statistics 2020. 2021.

[3] DNV-OS-J101. DNV-OS-J101-Design of offshore wind turbine structures. Copenhagen, Denmark: DNV; 2014.

[4] IEC-61400-1. Wind energy generation systems-part 1: design requirements. IEC; 2019. p. 61400–1. Ed 30.

[5] Arany L, Bhattacharya S, Macdonald JH, Hogan SJ. Closed form solution of Eigen frequency of monopile supported offshore wind turbines in deeper waters incorporating stiffness of substructure and SSI. Soil Dynam Earthq Eng 2016;83:18–32.

[6] Chen X, Xu JZ. Structural failure analysis of wind turbines impacted by super typhoon Usagi. Eng Fail Anal 2016;60:391–404.

[7] weblink. https://www.offshorewind.biz/2022/12/02/monopile-damaged-by-rogue-ship-to-be-removed-contractor-wanted.

[8] Fjellvikås Solvik K. Ship collision and earthquake analysis of monopile offshore wind turbines. NTNU; 2020.

[9] Ladeira I, Le Sourne H, Moran J, Salazar P. A semi-analytical methodology to assess the dynamic elastic response of a monopile offshore wind turbine subjected to low-energy ship impacts. In: International conference on offshore mechanics and arctic engineering. American Society of Mechanical Engineers; 2022, V002T02A12.

[10] weblink. https://mothersagainstturbines.com/2016/04/07/2016-wind-turbine-accident-report/comment-page-1/.

[11] IEC-61400-1. International electrotechnical commission wind turbines-part 1: design requirements. 2005. IEC 614001 Ed 3.

[12] van der Tempel J, Molenaar D-P. Wind turbine structural dynamics–a review of the principles for modern power generation, onshore and offshore. Wind Eng 2002;26:211–22.

[13] Ko Y-Y. A simplified structural model for monopile-supported offshore wind turbines with tapered towers. Renew Energy 2020;156:777–90.

[14] API-RPGEO. Petroleum and natural gas industries—specific requirements for offshore structures, Part 4—geotechnical and foundation design considerations. Washington, DC: American Petroleum Institute; 2016.

[15] DNV-ST-0126. DNVGL-ST-0126: support structures for wind turbines. Oslo, Norway: DNV GL; 2016.

[16] Shadlou M, Bhattacharya S. Dynamic stiffness of monopiles supporting offshore wind turbine generators. Soil Dynam Earthq Eng 2016;88:15–32.

[17] Abdel-Rahman K, Achmus M. Finite element modelling of horizontally loaded monopile foundations for offshore wind energy converters in Germany. In: Proceedings of the international symposium on frontiers in offshore geotechnics. Perth: Taylor and Francis; 2005. p. 391–6.

[18] Bir G, Jonkman J. Modal dynamics of large wind turbines with different support structures. In: International conference on offshore mechanics and arctic engineering; 2008. p. 669–79.

[19] Zaaijer M. Foundation modelling to assess dynamic behaviour of offshore wind turbines. Appl Ocean Res 2006;28:45–57.

[20] Arany L, Bhattacharya S, Adhikari S, Hogan S, Macdonald JHG. An analytical model to predict the natural frequency of offshore wind turbines on three-spring flexible foundations using two different beam models. Soil Dynam Earthq Eng 2015;74:40–5.

[21] Robinson MTA, Wang Z. The effect of the TMD on the vibration of an offshore wind turbine considering three soil-pile-interaction models. Adv Struct Eng 2021; 24:2652–68.

[22] Randolph MF. The response of flexible piles to lateral loading. Geotechnique 1981;31:247–59.

[23] Carter JP, Kulhawy FH. Analysis of laterally loaded shafts in rock. Journal of Geotechnical Engineering 1992;118:839–55.

[24] Poulos HG, Davis EH. Pile foundation analysis and design. New York: Wiley; 1980.

[25] Arany L, Bhattacharya S, Macdonald J, Hogan S. Design of monopiles for offshore wind turbines in 10 steps. Soil Dynam Earthq Eng 2017;92:126–52.

[26] Langen I, Sigbjörnsson R. Dynamisk analyse av konstruksjoner: dynamic analysis of structures. Tapir; 1979.

[27] Erturk A, Inman D. Appendix c: modal analysis of a uniform cantilever with a tip mass. Piezoelectric Energy Harvesting 2011:353–66.

[28] Jonkman J, Butterfield S, Musial W, Scott G. Definition of a 5-MW reference wind turbine for offshore system development. Golden, CO (United States): National Renewable Energy Lab.(NREL); 2009.

[29] Bak C, Zahle F, Bitsche R, Kim T, Yde A, Henriksen LC, et al. Description of the DTU 10 MW reference wind turbine. DTU Wind Energy Report-I-0092 2013;5.

[30] Bachynski EE, Ormberg H. Hydrodynamic modeling of large-diameter bottom-fixed offshore wind turbines. In: International conference on offshore mechanics and arctic engineering. American Society of Mechanical Engineers; 2015, V009T09A51.

[31] Soreide T, Amdahl J, Eberg E, Hellan O, Halmås T. USFOS–a computer program for progressive collapse analysis of steel offshore structures. Theory Manual SINTEF Report STF71 F. 1999:88038.

[32] Yu Z, Amdahl J, Rypestøl M, Cheng Z. Numerical modelling and dynamic response analysis of a 10 MW semi-submersible floating offshore wind turbine subjected to ship collision loads. Renew Energy 2022;184:677–99.

[33] Yu Z, Amdahl J. A review of structural responses and design of offshore tubular structures subjected to ship impacts. Ocean Eng 2018;154:177–203.

[34] Sha Y, Amdahl J, Dørum C. Local and global responses of a floating bridge under ship–girder collisions. J Offshore Mech Arctic Eng 2019;141:031601.

[35] Yu Z, Amdahl J, Kristiansen D, Bore PT. Numerical analysis of local and global responses of an offshore fish farm subjected to ship impacts. Ocean Eng 2019;194: 106653.

[36] USFOS. USFOS manual: modelling of large diameter piles in USFOS. 2019.

[37] USFOS. Modelling of large diameter piles in USFOS. 2019.

[38] Psaroudakis E, Mylonakis G, Klimis N. Non-linear analysis of laterally loaded piles using" py" curves. Geotech Geol Eng 2021;39:1541–56.

[39] Smilden E, Sørum SH, Bachynski EE, Sørensen AJ, Amdahl J. Post-installation adaptation of offshore wind turbine controls. Wind Energy 2020;23:967–85.

[40] Horn J-T. Statistical and modelling uncertainties in the design of offshore wind turbines. 2018.

[41] API-RPGEO. Api. RPGEO Geotechnical Foundation Design Considerations; April; 2011.

[42] Darvishi-Alamouti S, Bahaari M-R, Moradi M. Natural frequency of offshore wind turbines on rigid and flexible monopiles in cohesionless soils with linear stiffness distribution. Appl Ocean Res 2017;68:91–102.